EUROPEAN LABORATORY FOR PARTICLE PHYSICS

CERN-EP/98-173
27th October 1998

Search for Higgs Bosons in e^+e^- Collisions at 183 GeV

The OPAL Collaboration

Abstract

The data collected by the OPAL experiment at $\sqrt{s} = 183$ GeV were used to search for Higgs bosons which are predicted by the Standard Model and various extensions, such as general models with two Higgs field doublets and the Minimal Supersymmetric Standard Model (MSSM). The data correspond to an integrated luminosity of approximately 54 pb^{-1}. None of the searches for neutral and charged Higgs bosons have revealed an excess of events beyond the expected background. This negative outcome, in combination with similar results from searches at lower energies, leads to new limits for the Higgs boson masses and other model parameters. In particular, the 95% confidence level lower limit for the mass of the Standard Model Higgs boson is 88.3 GeV. Charged Higgs bosons can be excluded for masses up to 59.5 GeV. In the MSSM, $m_{\mathrm{h}^0} > 70.5$ GeV and $m_{\mathrm{A}^0} > 72.0$ GeV are obtained for $\tan\beta > 1$, no and maximal scalar top mixing and soft SUSY-breaking masses of 1 TeV. The range $0.8 < \tan\beta < 1.9$ is excluded for minimal scalar top mixing and $m_{\mathrm{top}} \leq 175$ GeV. More general scans of the MSSM parameter space are also considered.

(Submitted to the European Physical Journal C)

The OPAL Collaboration

G. Abbiendi[2], K. Ackerstaff[8], G. Alexander[23], J. Allison[16], N. Altekamp[5], K.J. Anderson[9], S. Anderson[12], S. Arcelli[17], S. Asai[24], S.F. Ashby[1], D. Axen[29], G. Azuelos[18,a], A.H. Ball[17], E. Barberio[8], R.J. Barlow[16], R. Bartoldus[3], J.R. Batley[5], S. Baumann[3], J. Bechtluft[14], T. Behnke[27], K.W. Bell[20], G. Bella[23], A. Bellerive[9], S. Bentvelsen[8], S. Bethke[14], S. Betts[15], O. Biebel[14], A. Biguzzi[5], S.D. Bird[16], V. Blobel[27], I.J. Bloodworth[1], P. Bock[11], J. Böhme[14], D. Bonacorsi[2], M. Boutemeur[34], S. Braibant[8], P. Bright-Thomas[1], L. Brigliadori[2], R.M. Brown[20], H.J. Burckhart[8], P. Capiluppi[2], R.K. Carnegie[6], A.A. Carter[13], J.R. Carter[5], C.Y. Chang[17], D.G. Charlton[1,b], D. Chrisman[4], C. Ciocca[2], P.E.L. Clarke[15], E. Clay[15], I. Cohen[23], J.E. Conboy[15], O.C. Cooke[8], C. Couyoumtzelis[13], R.L. Coxe[9], M. Cuffiani[2], S. Dado[22], G.M. Dallavalle[2], R. Davis[30], S. De Jong[12], A. de Roeck[8], P. Dervan[15], K. Desch[8], B. Dienes[33,d], M.S. Dixit[7], J. Dubbert[34], E. Duchovni[26], G. Duckeck[34], I.P. Duerdoth[16], D. Eatough[16], P.G. Estabrooks[6], E. Etzion[23], F. Fabbri[2], M. Fanti[2], A.A. Faust[30], F. Fiedler[27], M. Fierro[2], I. Fleck[8], R. Folman[26], A. Fürtjes[8], D.I. Futyan[16], P. Gagnon[7], J.W. Gary[4], J. Gascon[18], S.M. Gascon-Shotkin[17], G. Gaycken[27], C. Geich-Gimbel[3], G. Giacomelli[2], P. Giacomelli[2], V. Gibson[5], W.R. Gibson[13], D.M. Gingrich[30,a], D. Glenzinski[9], J. Goldberg[22], W. Gorn[4], C. Grandi[2], K. Graham[28], E. Gross[26], J. Grunhaus[23], M. Gruwé[27], G.G. Hanson[12], M. Hansroul[8], M. Hapke[13], K. Harder[27], A. Harel[22], C.K. Hargrove[7], C. Hartmann[3], M. Hauschild[8], C.M. Hawkes[1], R. Hawkings[27], R.J. Hemingway[6], M. Herndon[17], G. Herten[10], R.D. Heuer[27], M.D. Hildreth[8], J.C. Hill[5], P.R. Hobson[25], M. Hoch[18], A. Hocker[9], K. Hoffman[8], R.J. Homer[1], A.K. Honma[28,a], D. Horváth[32,c], K.R. Hossain[30], R. Howard[29], P. Hüntemeyer[27], P. Igo-Kemenes[11], D.C. Imrie[25], K. Ishii[24], F.R. Jacob[20], A. Jawahery[17], H. Jeremie[18], M. Jimack[1], C.R. Jones[5], P. Jovanovic[1], T.R. Junk[6], D. Karlen[6], V. Kartvelishvili[16], K. Kawagoe[24], T. Kawamoto[24], P.I. Kayal[30], R.K. Keeler[28], R.G. Kellogg[17], B.W. Kennedy[20], D.H. Kim[19], A. Klier[26], S. Kluth[8], T. Kobayashi[24], M. Kobel[3,e], D.S. Koetke[6], T.P. Kokott[3], M. Kolrep[10], S. Komamiya[24], R.V. Kowalewski[28], T. Kress[4], P. Krieger[6], J. von Krogh[11], T. Kuhl[3], P. Kyberd[13], G.D. Lafferty[16], H. Landsman[22], D. Lanske[14], J. Lauber[15], S.R. Lautenschlager[31], I. Lawson[28], J.G. Layter[4], D. Lazic[22], A.M. Lee[31], D. Lellouch[26], J. Letts[12], L. Levinson[26], R. Liebisch[11], B. List[8], C. Littlewood[5], A.W. Lloyd[1], S.L. Lloyd[13], F.K. Loebinger[16], G.D. Long[28], M.J. Losty[7], J. Ludwig[10], D. Liu[12], A. Macchiolo[2], A. Macpherson[30], W. Mader[3], M. Mannelli[8], S. Marcellini[2], C. Markopoulos[13], A.J. Martin[13], J.P. Martin[18], G. Martinez[17], T. Mashimo[24], P. Mättig[26], W.J. McDonald[30], J. McKenna[29], E.A. Mckigney[15], T.J. McMahon[1], R.A. McPherson[28], F. Meijers[8], S. Menke[3], F.S. Merritt[9], H. Mes[7], J. Meyer[27], A. Michelini[2], S. Mihara[24], G. Mikenberg[26], D.J. Miller[15], R. Mir[26], W. Mohr[10], A. Montanari[2], T. Mori[24], K. Nagai[8], I. Nakamura[24], H.A. Neal[12], B. Nellen[3], R. Nisius[8], S.W. O'Neale[1], F.G. Oakham[7], F. Odorici[2], H.O. Ogren[12], M.J. Oreglia[9], S. Orito[24], J. Pálinkás[33,d], G. Pásztor[32], J.R. Pater[16], G.N. Patrick[20], J. Patt[10], R. Perez-Ochoa[8], S. Petzold[27], P. Pfeifenschneider[14], J.E. Pilcher[9], J. Pinfold[30], D.E. Plane[8], P. Poffenberger[28], J. Polok[8], M. Przybycień[8], C. Rembser[8], H. Rick[8], S. Robertson[28], S.A. Robins[22], N. Rodning[30], J.M. Roney[28], K. Roscoe[16], A.M. Rossi[2], Y. Rozen[22], K. Runge[10], O. Runolfsson[8], D.R. Rust[12], K. Sachs[10], T. Saeki[24], O. Sahr[34], W.M. Sang[25], E.K.G. Sarkisyan[23], C. Sbarra[29], A.D. Schaile[34], O. Schaile[34], F. Scharf[3], P. Scharff-Hansen[8], J. Schieck[11], B. Schmitt[8], S. Schmitt[11], A. Schöning[8], M. Schröder[8], M. Schumacher[3], C. Schwick[8], W.G. Scott[20], R. Seuster[14], T.G. Shears[8], B.C. Shen[4], C.H. Shepherd-Themistocleous[8], P. Sherwood[15], G.P. Siroli[2], A. Sittler[27], A. Skuja[17], A.M. Smith[8], G.A. Snow[17], R. Sobie[28], S. Söldner-Rembold[10], S. Spagnolo[20], M. Sproston[20], A. Stahl[3], K. Stephens[16], J. Steuerer[27], K. Stoll[10], D. Strom[19],

R. Ströhmer[34], B. Surrow[8], S.D. Talbot[1], S. Tanaka[24], P. Taras[18], S. Tarem[22], R. Teuscher[8], M. Thiergen[10], J. Thomas[15], M.A. Thomson[8], E. von Törne[3], E. Torrence[8], S. Towers[6], I. Trigger[18], Z. Trócsányi[33], E. Tsur[23], A.S. Turcot[9], M.F. Turner-Watson[1], I. Ueda[24], R. Van Kooten[12], P. Vannerem[10], M. Verzocchi[10], H. Voss[3], F. Wäckerle[10], A. Wagner[27], C.P. Ward[5], D.R. Ward[5], P.M. Watkins[1], A.T. Watson[1], N.K. Watson[1], P.S. Wells[8], N. Wermes[3], J.S. White[6], G.W. Wilson[16], J.A. Wilson[1], T.R. Wyatt[16], S. Yamashita[24], G. Yekutieli[26], V. Zacek[18], D. Zer-Zion[8]

[1]School of Physics and Astronomy, University of Birmingham, Birmingham B15 2TT, UK
[2]Dipartimento di Fisica dell' Università di Bologna and INFN, I-40126 Bologna, Italy
[3]Physikalisches Institut, Universität Bonn, D-53115 Bonn, Germany
[4]Department of Physics, University of California, Riverside CA 92521, USA
[5]Cavendish Laboratory, Cambridge CB3 0HE, UK
[6]Ottawa-Carleton Institute for Physics, Department of Physics, Carleton University, Ottawa, Ontario K1S 5B6, Canada
[7]Centre for Research in Particle Physics, Carleton University, Ottawa, Ontario K1S 5B6, Canada
[8]CERN, European Organisation for Particle Physics, CH-1211 Geneva 23, Switzerland
[9]Enrico Fermi Institute and Department of Physics, University of Chicago, Chicago IL 60637, USA
[10]Fakultät für Physik, Albert Ludwigs Universität, D-79104 Freiburg, Germany
[11]Physikalisches Institut, Universität Heidelberg, D-69120 Heidelberg, Germany
[12]Indiana University, Department of Physics, Swain Hall West 117, Bloomington IN 47405, USA
[13]Queen Mary and Westfield College, University of London, London E1 4NS, UK
[14]Technische Hochschule Aachen, III Physikalisches Institut, Sommerfeldstrasse 26-28, D-52056 Aachen, Germany
[15]University College London, London WC1E 6BT, UK
[16]Department of Physics, Schuster Laboratory, The University, Manchester M13 9PL, UK
[17]Department of Physics, University of Maryland, College Park, MD 20742, USA
[18]Laboratoire de Physique Nucléaire, Université de Montréal, Montréal, Quebec H3C 3J7, Canada
[19]University of Oregon, Department of Physics, Eugene OR 97403, USA
[20]CLRC Rutherford Appleton Laboratory, Chilton, Didcot, Oxfordshire OX11 0QX, UK
[22]Department of Physics, Technion-Israel Institute of Technology, Haifa 32000, Israel
[23]Department of Physics and Astronomy, Tel Aviv University, Tel Aviv 69978, Israel
[24]International Centre for Elementary Particle Physics and Department of Physics, University of Tokyo, Tokyo 113-0033, and Kobe University, Kobe 657-8501, Japan
[25]Institute of Physical and Environmental Sciences, Brunel University, Uxbridge, Middlesex UB8 3PH, UK
[26]Particle Physics Department, Weizmann Institute of Science, Rehovot 76100, Israel
[27]Universität Hamburg/DESY, II Institut für Experimental Physik, Notkestrasse 85, D-22607 Hamburg, Germany
[28]University of Victoria, Department of Physics, P O Box 3055, Victoria BC V8W 3P6, Canada
[29]University of British Columbia, Department of Physics, Vancouver BC V6T 1Z1, Canada
[30]University of Alberta, Department of Physics, Edmonton AB T6G 2J1, Canada

[31]Duke University, Dept of Physics, Durham, NC 27708-0305, USA
[32]Research Institute for Particle and Nuclear Physics, H-1525 Budapest, P O Box 49, Hungary
[33]Institute of Nuclear Research, H-4001 Debrecen, P O Box 51, Hungary
[34]Ludwigs-Maximilians-Universität München, Sektion Physik, Am Coulombwall 1, D-85748 Garching, Germany

[a] and at TRIUMF, Vancouver, Canada V6T 2A3
[b] and Royal Society University Research Fellow
[c] and Institute of Nuclear Research, Debrecen, Hungary
[d] and Department of Experimental Physics, Lajos Kossuth University, Debrecen, Hungary
[e] on leave of absence from the University of Freiburg

1 Introduction

The OPAL detector at LEP collected in 1997 approximately 54 pb^{-1} of integrated luminosity at a centre-of-mass energy in the vicinity of 183 GeV. These data are used to search for neutral and charged Higgs bosons within the framework of the Standard Model (SM) [1], extensions with two Higgs field doublets (2HDM) [2], and the Minimal Supersymmetric extension of the Standard Model (MSSM) [3].

In the SM one Higgs boson, $\mathrm{H}^0_{\mathrm{SM}}$, is predicted with unspecified mass [4]. In $\mathrm{e}^+\mathrm{e}^-$ collisions at centre-of-mass energies accessible by LEP2, the $\mathrm{H}^0_{\mathrm{SM}}$ boson is expected to be produced predominantly via the "Higgs-strahlung" process $\mathrm{e}^+\mathrm{e}^-\to\mathrm{H}^0_{\mathrm{SM}}\mathrm{Z}^0$. Contributions from the $\mathrm{W}^+\mathrm{W}^-$ and $\mathrm{Z}^0\mathrm{Z}^0$ fusion processes account for a small part of the total production, except close to the kinematic limit of the $\mathrm{e}^+\mathrm{e}^-\to\mathrm{H}^0_{\mathrm{SM}}\mathrm{Z}^0$ process.

In any 2HDM, the Higgs sector comprises five physical Higgs bosons: two neutral CP-even scalars h^0 and H^0 (with masses satisfying $m_{\mathrm{h}^0} < m_{\mathrm{H}^0}$ by definition), one CP-odd scalar A^0 and two charged scalars $\mathrm{H}^\pm$. Our search is interpreted within the Type II Two Higgs Doublet Model without extra particles besides those of the SM and the two scalar doublets. In this model, the Higgs fields couple separately to up-type quarks for the first doublet, and to down-type quarks and charged leptons for the second doublet. At the current $\mathrm{e}^+\mathrm{e}^-$ centre-of-mass energies ($\sqrt{s}$) accessed by LEP, the h^0 and A^0 bosons are expected to be produced predominantly via two processes: the "Higgs-strahlung" process $\mathrm{e}^+\mathrm{e}^-\to\mathrm{h}^0\mathrm{Z}^0$ (as for $\mathrm{H}^0_{\mathrm{SM}}$) and the "pair production" process $\mathrm{e}^+\mathrm{e}^-\to\mathrm{h}^0\mathrm{A}^0$. For these two processes, the cross-sections σ_{hZ} and σ_{hA} are related at tree-level to the SM cross-sections [2]:

$$\mathrm{e}^+\mathrm{e}^-\to\mathrm{h}^0\mathrm{Z}^0 \ : \quad \sigma_{\mathrm{hZ}} = \sin^2(\beta-\alpha)\ \sigma^{\mathrm{SM}}_{\mathrm{HZ}}, \tag{1}$$

$$\mathrm{e}^+\mathrm{e}^-\to\mathrm{h}^0\mathrm{A}^0 \ : \quad \sigma_{\mathrm{hA}} = \cos^2(\beta-\alpha)\ \bar{\lambda}\ \sigma^{\mathrm{SM}}_{\nu\bar{\nu}}, \tag{2}$$

where $\sigma^{\mathrm{SM}}_{\mathrm{HZ}}$ and $\sigma^{\mathrm{SM}}_{\nu\bar{\nu}}$ are the cross-sections for the SM processes $\mathrm{e}^+\mathrm{e}^-\to\mathrm{H}^0_{\mathrm{SM}}\mathrm{Z}^0$ and $\mathrm{e}^+\mathrm{e}^-\to\nu\bar{\nu}$, and $\bar{\lambda}$ is a kinematic factor, depending on m_{h^0}, m_{A^0} and $\sqrt{s}$, typically having values between 0.5 and 0.7 for the centre-of-mass energies under consideration. The angle β is defined in terms of the vacuum expectation values v_1 and v_2 of the two scalar fields, $\tan\beta = v_2/v_1$, and α is the

mixing angle of the two CP-even fields. The coefficients $\sin^2(\beta-\alpha)$ and $\cos^2(\beta-\alpha)$ provide complementarity of the cross-sections for the two processes, a feature which is exploited in deriving bounds for Higgs boson masses and other model parameters. The MSSM is a model with two Higgs field doublets with precise predictions for the production cross-sections and Higgs boson decay branching ratios for a given set of MSSM model parameters.

Charged Higgs bosons are expected to be pair-produced in the reaction $e^+e^-\to H^+H^-$. The cross-section for this reaction in the 2HDM is completely determined by SM parameters for a given charged Higgs mass. However, the $H^\pm$ branching ratio is model-dependent. While in the MSSM, even with radiative corrections included [5], $m_{H^\pm} < m_{W^\pm}$ is barely possible, there are non-minimal models, e.g. with R-parity violation [6], which allow the charged Higgs boson to be lighter than the W-boson.

In this search, the dominant decays for neutral Higgs bosons, $H^0\to b\bar{b}$ and $H^0\to\tau^+\tau^-$ are considered. In the MSSM, the decay $h^0\to A^0A^0$ is also searched for where it is kinematically allowed. Higgs boson decays into SUSY particles are not searched for in this paper. For charged Higgs bosons, both the decay into $q\overline{q}'$ and into $\tau\nu_\tau$ are considered.

The OPAL search for H^0_{SM} at centre-of-mass energies ranging from m_{Z^0} to 172 GeV has resulted in a lower bound on its mass of $m_{H^0} > 69.4$ GeV at the 95% confidence level (CL) [7]. Previous OPAL searches for neutral Higgs bosons in 2HDM and the MSSM for $\sqrt{s} \leq 172$ GeV have been reported in [8]. For charged Higgs bosons, the published OPAL limit for $\sqrt{s} \leq 172$ GeV is $m_{H^\pm} > 52$ GeV at 95% CL [9].

Recent searches performed by the other LEP collaborations are listed in [10] for neutral Higgs bosons and in [11] for charged Higgs bosons. The CLEO and CDF collaborations have set more stringent limits on the mass of the charged Higgs bosons [12, 13] which are valid under certain model assumptions. The combined mass limit for the SM Higgs boson using data taken at $\sqrt{s} \leq 172$ GeV by the four LEP experiments is reported in [14].

Section 2 contains a short description of the OPAL detector, the data samples used, and the various Monte Carlo simulations. Section 3 gives a description of the procedure for tagging b-flavoured jets. The event selections for $H^0_{SM}Z^0$, h^0Z^0, h^0A^0, and H^+H^- are described in Sections 4, 5, and 6. The interpretation of the searches within the SM, 2HDM, and MSSM is presented in Section 7. Here also a model-independent interpretation of the neutral Higgs boson searches is given. In many cases, the results are combined with earlier search results [8, 9].

2 Experimental Considerations

The present analysis is based on data collected with the OPAL detector [15] during 1997 at an average luminosity weighted centre-of-mass energy of 182.7 GeV corresponding to an integrated luminosity of approximately[1] 54 pb^{-1}.

The OPAL experiment has nearly complete solid angle coverage and excellent hermeticity.

[1]Due to different requirements on the operation of the OPAL subdetectors the precise integrated luminosity differs from one search channel to the other.

The central tracking detector consists of a high-resolution silicon microstrip vertex detector (μVTX) [16] with polar angle[2] coverage $|\cos\theta| < 0.9$, which immediately surrounds the beam-pipe. It is followed by a high-precision vertex drift chamber, a large-volume jet chamber, and z–chambers to measure the z coordinate of tracks, all in a uniform 0.435 T axial magnetic field. The lead-glass electromagnetic calorimeter with presampler is located outside the magnet coil which provides, in combination with the forward calorimeter, gamma catcher, MIP plug [17], and silicon-tungsten luminometer [18], a geometrical acceptance down to 33 mrad from the beam direction. The silicon-tungsten luminometer serves to measure the integrated luminosity using small-angle Bhabha scattering events [19]. The magnet return yoke is instrumented with streamer tubes and thin gap chambers for hadron calorimetry; it is surrounded by several layers of muon chambers.

Events are reconstructed from charged-particle tracks and energy deposits ("clusters") in the electromagnetic and hadron calorimeters. The tracks and clusters must pass a set of quality requirements similar to those used in previous OPAL Higgs boson searches [20]. In calculating the total visible energies and momenta, $E_{\rm vis}$ and $\vec{P}_{\rm vis}$, of events and individual jets, corrections are applied to prevent double-counting of energy in the case of tracks and associated clusters [21].

The signal detection efficiencies and accepted background cross-sections are estimated using a variety of Monte Carlo samples. The HZHA generator [22] is used to simulate Higgs boson production processes. The detection efficiencies are determined at fixed values of Higgs boson masses using sample sizes varying between 500 and 10,000 events. Efficiencies at arbitrary masses are evaluated using spline fits in $m_{\rm H^0}$, $m_{\rm H^\pm}$ or in the $(m_{\rm h^0}, m_{\rm A^0})$ plane. The background processes are simulated primarily by the following event generators: PYTHIA [23] ($(\rm Z/\gamma)^* \to q\bar{q}(\gamma)$), EXCALIBUR [24] and grc4f [25] (four-fermion processes (4f)), BHWIDE [26] ($\rm e^+e^-(\gamma)$), KORALZ [27] ($\mu^+\mu^-(\gamma)$ and $\tau^+\tau^-(\gamma)$), and PHOJET [28], HERWIG [29], and Vermaseren [30] (hadronic and leptonic two-photon processes ($\gamma\gamma$)). The generated partons are hadronised using JETSET [23] with parameters described in [31]. For systematic studies, cluster fragmentation implemented in HERWIG is also used. The resulting particles are processed through a full simulation of the OPAL detector [32].

3 Tagging of b-jets

Since neutral Higgs bosons decay preferentially to $\rm b\bar{b}$ pairs, the tagging of jets originating from b-quarks plays an important role in Higgs boson searches. A jet-wise b-tagging algorithm has been developed using three independent b-tagging methods: (1) lifetime tag, (2) high-$p_{\rm t}$ lepton tag, and (3) jet shape tag. These three methods, described below, are combined using an unbinned likelihood method to form a single discriminating variable for each jet.

(1) The lifetime tag exploits the relatively long lifetime, high decay multiplicity and high mass of the b-flavoured hadrons. Five quantities are calculated from the tracks and

[2]OPAL uses a right-handed coordinate system where the $+z$ direction is along the electron beam and where $+x$ points to the centre of the LEP ring. The polar angle, θ, is defined with respect to the $+z$ direction and the azimuthal angle, ϕ, with respect to the horizontal, $+x$ direction.

clusters assigned to a given jet. These five quantities are input to an artificial neural network (ANN) to form a lifetime tag, β_τ, for each jet considered. Figure 1(a) shows the distribution of β_τ in the central detector region for $Z^0 \to q\bar{q}$ events for OPAL data at $\sqrt{s} = m_{Z^0}$ together with the Monte Carlo simulation. Details are given in the Appendix.

(2) Semileptonic b-decays are identified using electron and muon selections, rejecting electrons from γ conversions as described in [33]. The transverse momentum p_t^ℓ of the lepton, calculated with respect to the direction of the sub-jet (see Appendix) which includes the lepton track, is used as a b-tag variable. Figure 1(b) shows the p_t^ℓ spectrum of the tagged leptons for $Z^0 \to q\bar{q}$ events for OPAL data at $\sqrt{s} = m_{Z^0}$ together with the Monte Carlo simulation.

(3) The larger decay multiplicity and higher mass of the b-flavoured hadrons tend to result in a more spherical shape for b-jets compared to lighter flavour jets. As a measure of the jet shape, the boosted sphericity β_s, defined as the sphericity of the jet calculated in its rest frame, is used as a jet shape tag. The distribution of β_s is shown in Figure 1(c).

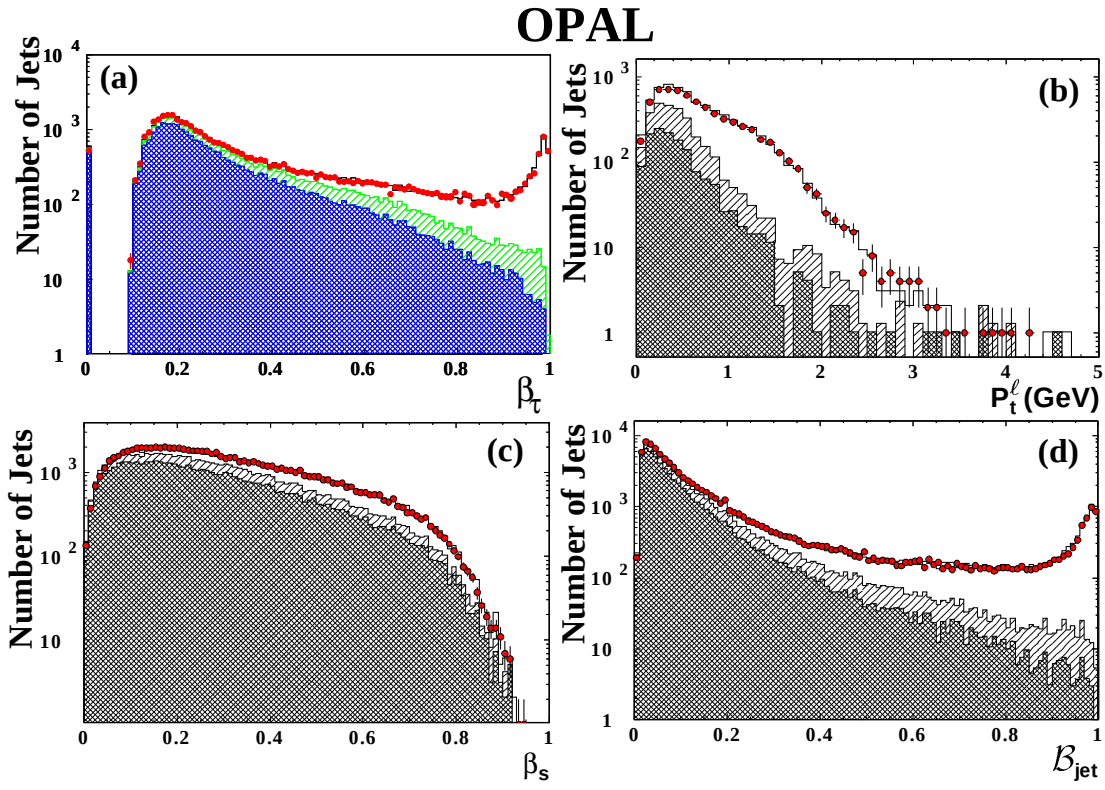

Figure 1: *(a) Lifetime tag β_τ (ANN output) for central detector region $|\cos\theta_{jet}| \leq 0.75$; (b) p_t^ℓ -distribution for events with tagged leptons; (c) distribution of boosted sphericity, β_s; (d) distribution of $\mathcal{B}_{jet}$. The histograms are Monte Carlo simulations of $Z^0 \to q\bar{q}$ decays for different flavours (cross-hatched: uds flavour; hatched: c flavour; open: b-flavour); the dots with error bars are OPAL data taken in 1997 at $\sqrt{s} = m_{Z^0}$.*

Since the three quantities described above, β_τ, p_t^ℓ, and β_s, exploit different properties of b-flavoured hadron decays which are almost uncorrelated, they are combined using an unbinned

likelihood method. The final b-tagging discriminant $\mathcal{B}_{\rm jet}$, defined as

$$\mathcal{B}_{\rm jet} = \frac{w_{\rm b} \cdot f^{\tau}_{\rm b} \cdot f^{\ell}_{\rm b} \cdot f^{s}_{\rm b}}{w_{\rm b} \cdot f^{\tau}_{\rm b} \cdot f^{\ell}_{\rm b} \cdot f^{s}_{\rm b} + w_{\rm c} \cdot f^{\tau}_{\rm c} \cdot f^{\ell}_{\rm c} \cdot f^{s}_{\rm c} + w_{\rm uds} \cdot f^{\tau}_{\rm uds} \cdot f^{\ell}_{\rm uds} \cdot f^{s}_{\rm uds}}, \tag{3}$$

is calculated for each jet. Here, $w_{\rm b}$, $w_{\rm c}$, and $w_{\rm uds}$ are weight factors to accommodate different flavour compositions of the background in different search channels. It has been found, however, that the sensitivity does not strongly depend on the choice of these weight factors. The functions $f^{t}_{\rm q}$ are the probability density functions for flavour q = b,c,uds for the tagging method $t = \tau, \ell, s$, determined from Monte Carlo. The distribution of the final b-tagging discriminant $\mathcal{B}_{jet}$ is shown in Figure 1(d). Good agreement can be seen between data and Monte Carlo simulation. The agreement has also been checked using data and Monte Carlo samples of $e^+e^-\to Z^0\gamma$ events at $\sqrt{s} = 183$ GeV. The efficiency of the algorithm has been verified from identified $Z^0\to b\bar{b}$ events at $\sqrt{s} = m_{Z^0}$ using the double tagging method described in [34].

4 Searches for $e^+e^-\to Z^0H^0$

The process $e^+e^-\to Z^0H^0$ is searched for in the following final states: $Z^0H^0\to q\bar{q}b\bar{b}$ (four jet channel), $Z^0H^0\to\nu\bar{\nu}b\bar{b}$ (missing energy channel), $Z^0H^0\to\tau^+\tau^-b\bar{b}$ and $Z^0H^0\to q\bar{q}\tau^+\tau^-$ (tau channels), $Z^0H^0\to e^+e^-b\bar{b}$ and $Z^0H^0\to\mu^+\mu^-b\bar{b}$ (electron and muon channels). Throughout this section H^0 denotes a "generic" neutral Higgs boson, i.e. $H^0_{\rm SM}$ in the SM and h^0 in the 2HDM and MSSM. A search for the process $Z^0h^0\to Z^0A^0A^0$ which is possible only in 2HDM and in the MSSM is also described in this section.

4.1 The Four Jet Channel

The process $e^+e^-\to Z^0H^0\to q\bar{q}b\bar{b}$ accounts for approximately 60% of the SM Higgs boson production cross-section. It is characterised by four energetic hadronic jets, large visible energy and the presence of b-hadron decays. The backgrounds are $(Z/\gamma)^*\to q\bar{q}$ with and without initial state radiation and hard gluon emission, as well as four-fermion processes, in particular, $W^+W^-\to q\overline{q}'q\overline{q}'$. The suppression of these backgrounds relies on the kinematic reconstruction of the Z^0 boson and on the identification of b-quarks from the Higgs boson decay. The tagging of jets containing b-flavoured hadrons proceeds as explained in Section 3.

The selection of candidate events is done in two steps. A preselection using cuts is first applied to retain only four-jet-like events. The preselection requires: (1) a hadronic final state [35], (2) an effective centre-of-mass energy [35], $\sqrt{s'}$, in excess of 150 GeV, (3) the jet resolution parameter in the Durham scheme [36], y_{34}, larger than 0.003, (4) the event shape C–parameter [37] larger than 0.25, (5) at least two charged particle tracks in each of the four jets, and (6) the 4-C fit (requiring energy and momentum conservation) and the 5-C fit (additionally constraining two jets to have an invariant mass of m_{Z^0}), as described in [7], must each yield a χ^2 probability larger than 10^{-5}.

Table 1 shows the number of events selected for the data and the Monte Carlo simulations of the various background processes at each stage of the cuts.

Cut	Data 183 GeV	Total bkg.	$q\bar{q}(\gamma)$	4f	$\gamma\gamma$	Efficiency (%) $m_{H^0} = 85$ GeV
(1)	6131	6153.3	5095.8	949.5	108.0	99.8
(2)	1956	1958.5	1404.6	548.7	5.2	94.5
(3)	711	677.2	254.1	421.0	2.1	91.7
(4)	683	656.1	234.1	420.0	2.0	91.4
(5)	576	563.8	192.5	369.9	1.4	88.2
(6)	514	498.2	159.4	338.4	0.4	85.6
$\mathcal{L}^{HZ} > 0.96$	7	4.95±0.23	1.8	3.1	-	39.2

Table 1: *The number of events after each cut of the selection for the data at* $\sqrt{s} = 183$ GeV *and the expected background in the four jet channel. The background estimates are normalised to the integrated luminosity corresponding to the data, 54.1* pb^{-1}*. The quoted error on the total background estimate is statistical. The last column shows the selection efficiencies for the* $Z^0H^0 \to q\bar{q}b\bar{b}$ *final state for a Higgs boson mass of 85 GeV.*

After the preselection, a likelihood technique [7] is employed to classify the remaining events as $(Z/\gamma)^* \to q\bar{q}$, four-fermion processes, or $Z^0H^0 \to q\bar{q}b\bar{b}$. To select signal events with low background, eight quantities are used. The first six variables exploit the different kinematics of the background and signal events: (1) the logarithm of y_{34} in the Durham scheme; (2) the C-parameter; (3) the logarithm of the probability of the 5-C fit in which the two jets with the smallest b-tagging discriminants $\mathcal{B}_i$ (see Section 3) are constrained to have an invariant mass of m_{Z^0}; (4) the logarithm of the probability of the best kinematic fit requiring energy and momentum conservation and both di-jet masses to be equal to the nominal W mass; (5) the difference between the largest and smallest jet energies; (6) $\beta_{\rm min}$: the minimum of $\beta_{\rm di-jet1} + \beta_{\rm di-jet2}$ for each of the three possible di-jet combinations, where $\beta_{\rm di-jet(i)}$ is the ratio of di-jet momentum and energy after the 4-C fit.

To tag jets with b-flavoured hadrons, the two largest b-tagging discriminants $\mathcal{B}_i$ complete the set of input variables ((7) and (8)) to the likelihood selection. The two b-tagging discriminants $\mathcal{B}_i$ are ordered by decreasing energy of the jets. In the calculation of $\mathcal{B}_i$, the weight factors have been set to $w_{\rm b} = w_{\rm c} = w_{\rm uds} = 1$ (see Section 3). The distributions for four of the eight input quantities are shown in Figure 2.

Figure 3 shows the distributions of the signal likelihood, $\mathcal{L}^{HZ}$, for the preselected events. It can be seen that the expected signal is concentrated at large values of the likelihood. Candidate events are selected by requiring $\mathcal{L}^{HZ} > 0.96$. The efficiency for $m_{H^0} = 85$ GeV is 39.2±0.2(stat.)±1.2(syst.) %. The signal selection efficiencies as a function of the H^0 mass are given in Table 15. The expected background is 1.8±0.2 events from $(Z/\gamma)^*$ and 3.1±0.2 events from four-fermion processes. Other sources of background are negligible. Seven candidate events are selected, consistent with a total expected background of 5.0±0.2(stat.)±0.6(syst.) events. Their likelihood values and candidate Higgs masses are listed in Table 2.

The results of the 5-C fit are used as a measure of m_{H^0}. For each candidate event there are 3 ways to combine the four final state jets into a pair of di-jets. For a given di-jet combination, each pair, in turn, is constrained to m_{Z^0} while the other pair is taken as a measure of m_{H^0}. The pair yielding the fit with the largest χ^2 probability is used. According to the signal Monte

Carlo, the correct di-jet pairing is obtained in 70% of the selected events. The fraction of times the correct di-jet assignments to m_{Z^0} and m_{H^0} are made is a strong function of m_{H^0}; for $m_{\mathrm{H}^0} = 85$ GeV, the correct assignment is made in 43% of the selected events.

The signal selection efficiencies (background estimates) are affected by the following uncertainties expressed in relative percentages: description of the kinematic variables used in the preselection and in the likelihood selection, 0.6% (2.3%); modelling of the kinematic fit probabilities, 1.4% (3.2%); tracking resolution modelling, 0.6% (7.8%); b-hadron charged decay multiplicity uncertainty [38], 1.7% (6.3%); uncertainty in the b-quark fragmentation function [39], 1.9% (5.2%). Different Monte Carlo generators have been used to evaluate the background from $(\mathrm{Z}/\gamma)^*$-events (HERWIG instead of PYTHIA) and four-fermion events (EXCALIBUR instead of grc4f), yielding an uncertainty of 4.3% on the background estimates. Adding the above sources in quadrature yields a $\pm 3.0\%$ ($\pm 12.7\%$) systematic error on the selection efficiency (background estimate). The additional error from Monte Carlo statistics is 1.8% (4.6%).

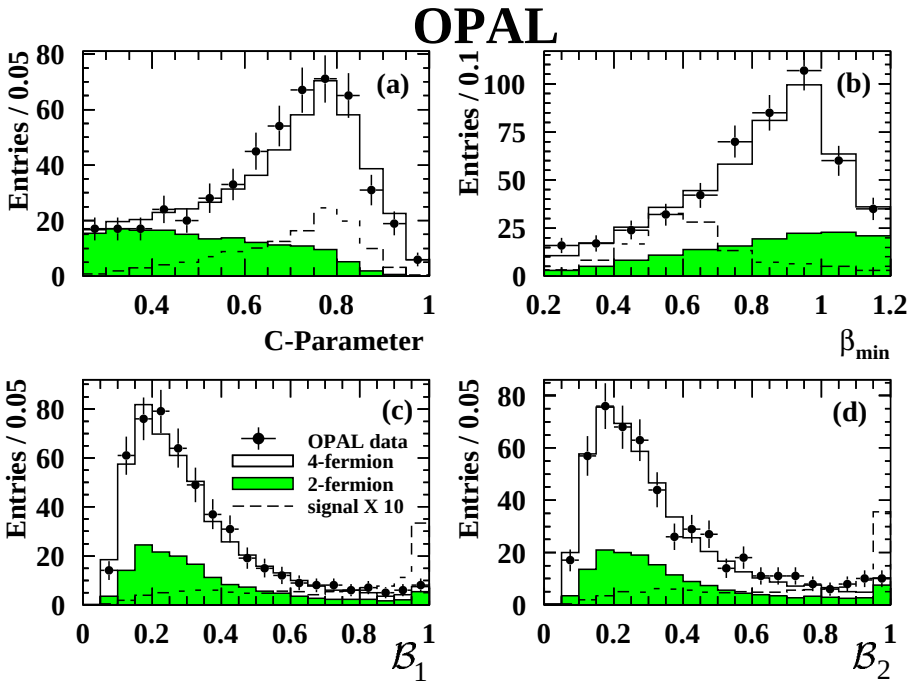

Figure 2: *Four jet channel: distribution of likelihood input variables (as described in the text) for data compared to Monte Carlo expectations. The points with error bars are OPAL data, the shaded (open) histogram is the simulation of* $(\mathrm{Z}/\gamma)^* \to \mathrm{q\bar{q}}$ *(four-fermion) events, normalised to the recorded luminosity. The dashed line is a simulated signal* (m_{H^0}*=85 GeV) scaled by a factor of 10 for better visibility.*

Event	1	2	3	4	5	6	7
$\mathcal{L}^{HZ}$	0.960	0.999	0.993	0.987	0.967	0.997	0.989
$\mathrm{m_{candidate}}$ (GeV)	52.5	67.9	72.4	75.6	78.9	82.9	89.1

Table 2: *The likelihood value and reconstructed mass of accepted candidates in the four-jet channel.*

As a cross check, an ANN selection for the four jet channel has been performed [40]. It proceeds through a preselection similar to the one used in the main analysis. Then a set of

discriminating variables is input to an ANN. The sensitivity is similar to the main analysis. As an example, for $m_{\mathrm{H}^0} = 85$ GeV the efficiency of this analysis is 37.2% with an expected background of 6.2±0.5 events. Of the selected simulated signal events, 80% are in common for both analyses. Of the accepted background cross-section for the main analysis, approximately 60% is also accepted by the ANN analysis. This is consistent with the observation that five of the six selected candidate events of the ANN analysis are shared with the likelihood analysis.

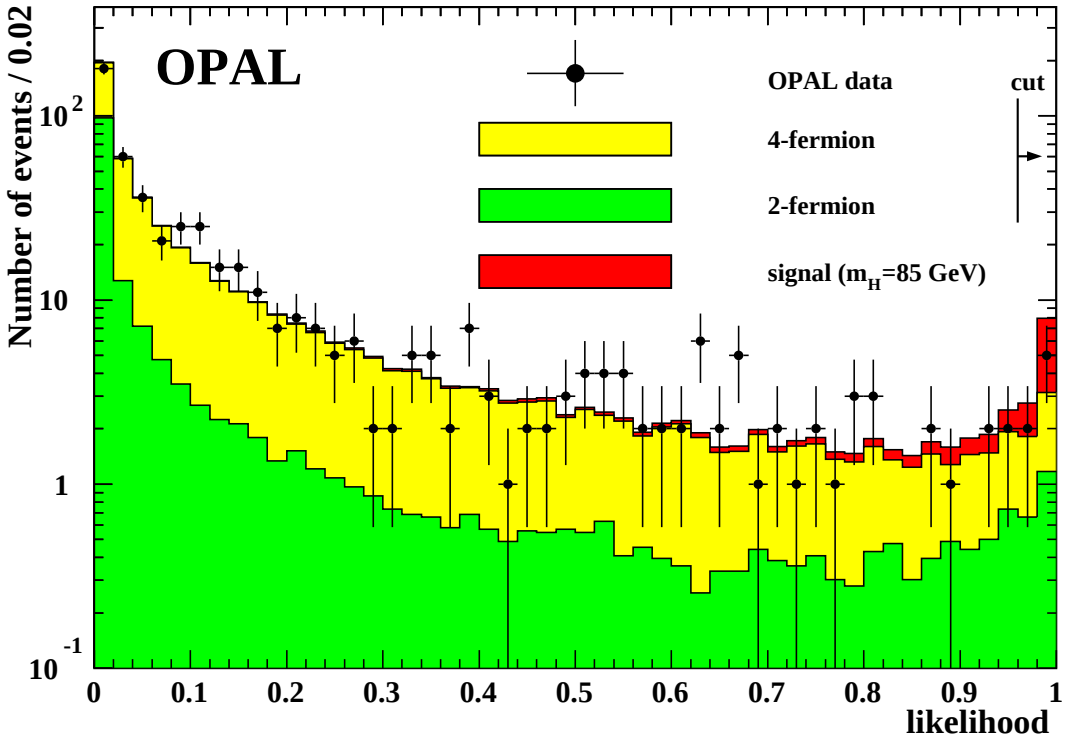

Figure 3: *Four jet channel: signal likelihood. The points with error bars are OPAL data, the light grey (dark grey) histogram is the simulation of* $(\mathrm{Z}/\gamma)^*\to\mathrm{q\bar{q}}$ *(four-fermion) events, normalised to the recorded luminosity. The black histogram represents a simulated signal* (m_{H^0}*=85 GeV) added to the expected background. The arrow indicates the position of the cut.*

4.2 The Missing Energy Channel

The $\mathrm{e^+e^-}\to\nu\bar{\nu}\mathrm{H}^0\to\nu\bar{\nu}\mathrm{b\bar{b}}$ process accounts for approximately 18% of the SM Higgs boson production cross-section with a small contribution (1.3% (relative) for m_{H^0}=85 GeV) from the $\mathrm{W^+W^-}$ fusion process. These events are characterised by large missing momentum and two energetic, acoplanar, b-flavoured jets. The dominant backgrounds are mis-measured $(\mathrm{Z}/\gamma)^*\to\mathrm{q\bar{q}}$ events, four-fermion processes with final state neutrinos such as $\mathrm{Z^0Z^{0*}}\to\nu\bar{\nu}\mathrm{q\bar{q}}$, $\mathrm{W^+W^-}\to\ell^{\pm}\nu\mathrm{q\bar{q}}$, $\mathrm{W^{\pm}e^{\mp}}\nu\to\mathrm{q\bar{q}e^{\mp}}\nu$ with the charged lepton escaping detection and, in general, events in which particles go undetected down the beam pipe such as $\mathrm{e^+e^-}\to\mathrm{Z^0}\gamma$ and two-photon events. For the latter backgrounds, the missing momentum vector points close to the beam direction, while signal events tend to have missing momentum in the transverse plane. The rest of the above mentioned backgrounds are largely reduced via b-tagging. The process $\mathrm{Z^0Z^{0*}}\to\nu\bar{\nu}\mathrm{b\bar{b}}$ remains an irreducible background.

The preselection requires: (1) the number of selected tracks [20] to be at least seven and at least 20% of the total number of tracks; no significant energy in the forward detectors as described in [7]; the fraction of energy in the region $|\cos\theta| > 0.90$ must not exceed 50% of the total visible energy, $E_{\rm vis}$; the total transverse momentum, $P^T_{\rm vis}$, must be greater than 8 GeV; the visible mass and energy must satisfy $m_{\rm vis} > 4$ GeV and $E_{\rm vis}/\sqrt{s} < 0.80$; (2) the polar angle, $\theta_{\rm miss}$, of the missing momentum ($\vec{P}_{\rm miss} = -\vec{P}_{\rm vis}$) must satisfy $|\cos\theta_{\rm miss}| < 0.95$ and the z-component of the visible momentum, $P^z_{\rm vis}$, is required to be less than 35 GeV; (3) the events are reconstructed as two-jet events using the Durham algorithm; both jet polar angles are required to satisfy $|\cos\theta_{\rm jet}| < 0.95$; (4) the acoplanarity angle $\phi_{\rm acop} = 180^\circ - \phi_{jj}$ (ϕ_{jj} is the angle between the two jets in the plane perpendicular to the beam axis) must be larger than 5°; (5) the missing mass $m_{\rm miss}$ is required to be consistent with $m_{\rm Z^0}$: $(60\ {\rm GeV})^2 < {\rm m}^2_{\rm miss} < (120\ {\rm GeV})^2$. (6) the event is required to have no isolated leptons as defined in [7]. The distributions of $\phi_{\rm acop}$ and $m^2_{\rm miss}$ are shown in Figs. 4(a) and (b).

Next, the b-tag (see Section 3) as well as some other kinematic requirements are incorporated into the analysis via a likelihood technique as described in [7]. Here, the information from six quantities (described below) is combined. The first set of variables entering the likelihood are all subject to loose cuts as part of the previously described preselection: (1) $|\cos\theta_{\rm miss}|$, (2) $\max|\cos\theta_{\rm jet}|$, (3) $m_{\rm miss}$ and (4) the acoplanarity angle. The remaining two variables are the b-tagging discriminants $\mathcal{B}_i$of jets 1 and 2, as defined in Section 3, ordered by decreasing jet energy. Since the dominant remaining backgrounds are $\rm q\bar{q}\ell\nu$ final states where the charged lepton is included in one of the hadronic jets, p^ℓ_t is not used in the calculation of $\mathcal{B}_i$. The weight factors have been set to $w_{\rm b} = w_{\rm c} = w_{\rm uds} = 1$. The distributions of these input variables are shown in Figures 4(c)-(h). In Figure 5, the resulting signal likelihood distributions are shown for the data and the Monte Carlo simulations. The signal likelihood is required to be larger than 0.60.

Cut	Data 183 GeV	Total bkg.	$\rm q\bar{q}(\gamma)$	4f	$\gamma\gamma$	Efficiency (%) $m_{\rm H^0} = 85$ GeV
(1)	806	737.5	457.8	273.3	6.4	74.9
(2)	348	310.4	91.6	215.0	3.8	72.9
(3)	322	295.4	86.0	205.6	3.8	70.8
(4)	217	209.6	16.9	189.5	3.2	65.0
(5)	52	45.6	6.1	38.7	0.8	62.5
(6)	25	26.4	5.3	20.3	0.8	60.6
$\mathcal{L}^{HZ} > 0.6$	0	1.56±0.13	0.29	1.27	0.0	40.2

Table 3: *The numbers of events after each cut for the data and the expected background for the missing energy channel. The background estimates are normalised to 53.9* $\rm pb^{-1}$. *The quoted error is statistical. The last column shows the selection efficiencies for the* $\nu\bar{\nu}(\rm H^0\rightarrow$ *all) final state for an 85 GeV Higgs boson.*

The numbers of observed and expected events after each selection cut are given in Table 3. No events survive the selection, while 1.56 ±0.13(stat.)±0.18(syst.) events are expected from SM background processes. The detection efficiencies as a function of the Higgs boson mass are listed in Table 15. In the calculation of the efficiencies and backgrounds a reduction by 3.7% (relative) has been applied in order to account for accidental vetos due to accelerator-related backgrounds in the forward detectors.

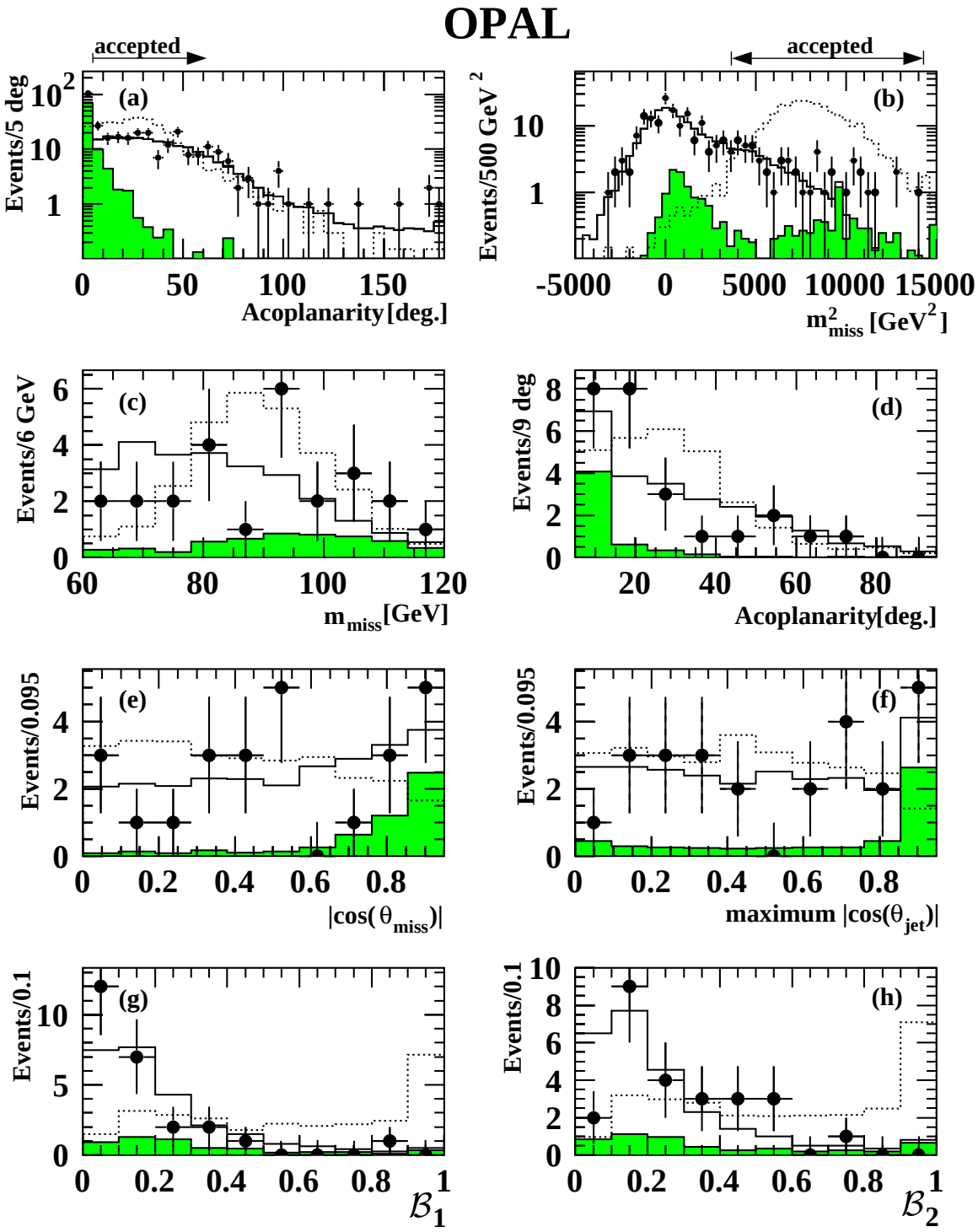

Figure 4: *Missing energy channel: (a) distributions of the acoplanarity angle after cut (3) and (b) missing mass squared after cut (4); (c)-(h) distribution of likelihood input variables after cuts (1)-(6). The points with error bars are OPAL data, the shaded (open) histogram represents the simulation of* $(Z/\gamma)^* \to q\bar{q}$ *(four-fermion) events normalised to the recorded luminosity. The dotted line represents a simulated signal* (m_{H^0}=*85 GeV) scaled by a factor of 100 in (a)–(b) and by a factor of 10 in (c)–(h) for better visibility.*

The systematic uncertainties due to modelling of the kinematic variables were estimated using WW $\rightarrow$ $q\overline{q}'\ell\nu$ and $e^+e^-\rightarrow q\bar{q}\gamma$ events where the identified isolated leptons or radiative photons were removed leaving a system with kinematical properties similar to those of 80–90 GeV Higgs bosons. The $q\overline{q}'\ell\nu$ events were also used to estimate the uncertainties in the isolated lepton tag. The detection efficiencies (number of expected background events) have the following uncertainties: modelling of the cut variables, 0.6% (0.8%); and lepton tag, 0.7% (0.8%); description of the tracking resolution, 0.2% (9.7%); uncertainty in the knowledge of the true b-decay multiplicity and energy 2.2% (5.8%). Adding the above systematic errors in quadrature, the total systematic uncertainty in the signal efficiency (background) is estimated to be 2.4% (11.4%). The additional error from Monte Carlo statistics is 0.8% (10%).

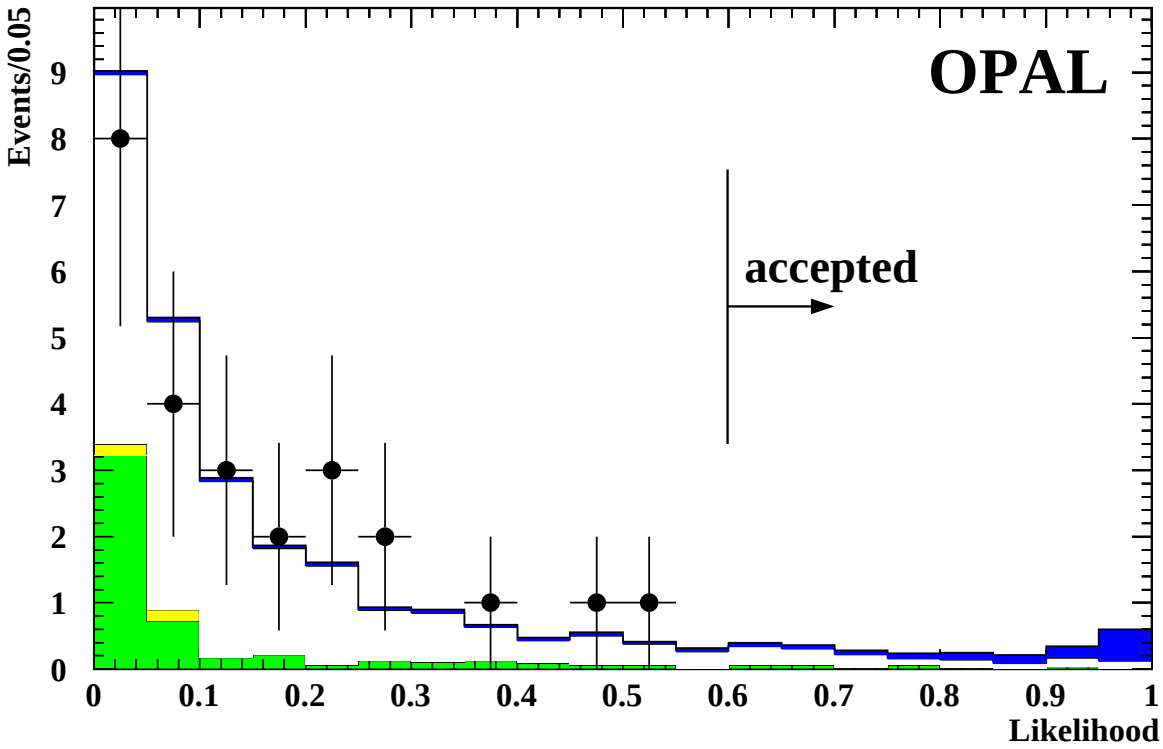

Figure 5: *The likelihood distribution for the missing energy channel. The points with error bars are OPAL data, the open histogram is the simulation of four-fermion processes and the grey (light grey) histogram is the simulation of* $(Z/\gamma)^*\rightarrow q\bar{q}$*–events (two-photon processes), all normalised to the recorded luminosity. The dark histogram is a simulated signal* (m_{H^0}=*85 GeV) added to the background expectation. The arrow indicates the position of the cut.*

4.3 The Tau Channels

The $q\bar{q}\tau^+\tau^-$final state accounts for approximately 9% of the total Z^0H^0 production rate (both the $(Z^0\rightarrow q\bar{q})(H^0\rightarrow\tau^+\tau^-)$ final state and the $(Z^0\rightarrow\tau^+\tau^-)(H^0\rightarrow q\bar{q})$ final state are considered) and is characterised by a pair of tau leptons and a pair of energetic hadronic jets. The background is suppressed by requiring that either the $\tau^+\tau^-$ or the $q\bar{q}$ pair yield a reconstructed invariant mass consistent with the Z^0 mass. The dominant backgrounds are the four-fermion

processes $Z^0Z^{0(*)} \to q\bar{q}\ell^+\ell^-$ and $W^+W^- \to q\bar{q}'\ell\nu$. The process $Z^0Z^{0*} \to \tau^+\tau^- b\bar{b}$ is an irreducible background.

The selection begins by identifying tau leptons in the event using an ANN. The ANN is a track-based algorithm used to discriminate real tau decay tracks from tracks arising from the hadronic system. The training process uses tracks from high momentum tau leptons (15 GeV$< p_\tau <$ 60 GeV) in simulated $q\bar{q}\tau^+\tau^-$ events as signal and tracks in $e^+e^- \to q\bar{q}$ events as background. Any track with momentum greater than 2 GeV and with no other good track within a cone of half-angle 10° is considered a one-prong tau candidate. Any family of three charged tracks within a 10° cone centred on any one of the tracks, having a total charge of ± 1, and a total momentum greater than 2 GeV is considered as a three-prong tau candidate. Each candidate is then used as input to the ANN.

The ANN was trained separately for one-prong and three-prong tau decays. Around each candidate an annular isolation cone of half-angle 30° is constructed concentric with and excluding the narrow 10° cone. Both the one-prong and three-prong ANN use as inputs the invariant mass of all tracks and neutral clusters in the 10° cone, the ratio of total energy contained in the isolation cone to that in the 10° cone, and the total number of tracks and neutral clusters with energy greater than 750 MeV in the isolation cone. The one-prong net additionally takes as input the total energy in the 10° cone, and the track energy in the isolation cone. The three-prong ANN additionally uses the largest angle between the most energetic track and any other track in the 10° cone. Figure 6 demonstrates the power of the ANN by comparing the two oppositely charged candidates with the largest ANN outputs in signal $q\bar{q}\tau^+\tau^-$events to those in SM background events.

The modelling of the fake rates is studied using high statistics $e^+e^- \to q\bar{q}$ data sets taken at $\sqrt{s} \approx m_{Z^0}$. The modelling of the signal inputs is studied using mixed events which are constructed by overlaying $e^+e^- \to q\bar{q}$ events with single hemispheres of $e^+e^- \to \tau^+\tau^-$ events at $\sqrt{s} \approx m_{Z^0}$. These mixed events are topologically and kinematically analogous to $q\bar{q}\tau\nu$ events at $\sqrt{s} \approx 183$ GeV. The systematic errors estimated from these studies are $\pm 10\%$ and $\pm 3\%$ for the fake rate and tau lepton efficiency, respectively.

For each event, pairs of oppositely charged tau candidates are used to construct a two-tau likelihood, $\mathcal{L}_{\tau\tau} = \frac{P_1 P_2}{P_1 P_2 + (1-P_1)(1-P_2)}$, where P_i is the probability that the ith tau-candidate originates from a real tau lepton. This probability is calculated using the shape of the ANN output for signal and fake events and the accepted fake rate estimated from Monte Carlo. The tau pair for the event is chosen to be that pair that maximises $\mathcal{L}_{\tau\tau}$.

The selection uses a likelihood technique to discriminate between candidate $H^0Z^0 \to q\bar{q}\tau^+\tau^-$ signal events and SM background processes. Before constructing the likelihood, the following preselection is made: the event is required to satisfy the high multiplicity selection described in [35], the number of charged tracks passing additional quality cuts must exceed six; the total visible energy, divided by $\sqrt{s}$, $R_{\rm vis}$, must exceed 0.32; the total missing momentum in the event divided by $\sqrt{s}$ must not exceed 0.40; the total scalar sum of momenta transverse to the beam axis must exceed 40 GeV; and the polar angle of the missing momentum vector, $\theta_{\rm miss}$, must satisfy $|\cos\theta_{\rm miss}| < 0.95$. After this preselection, the two-tau likelihood, $\mathcal{L}_{\tau\tau}$, is required to exceed 0.10. A 2-C kinematic fit is then performed which requires energy and momentum conservation. The directions of the tau lepton momenta is approximated by those of the visible

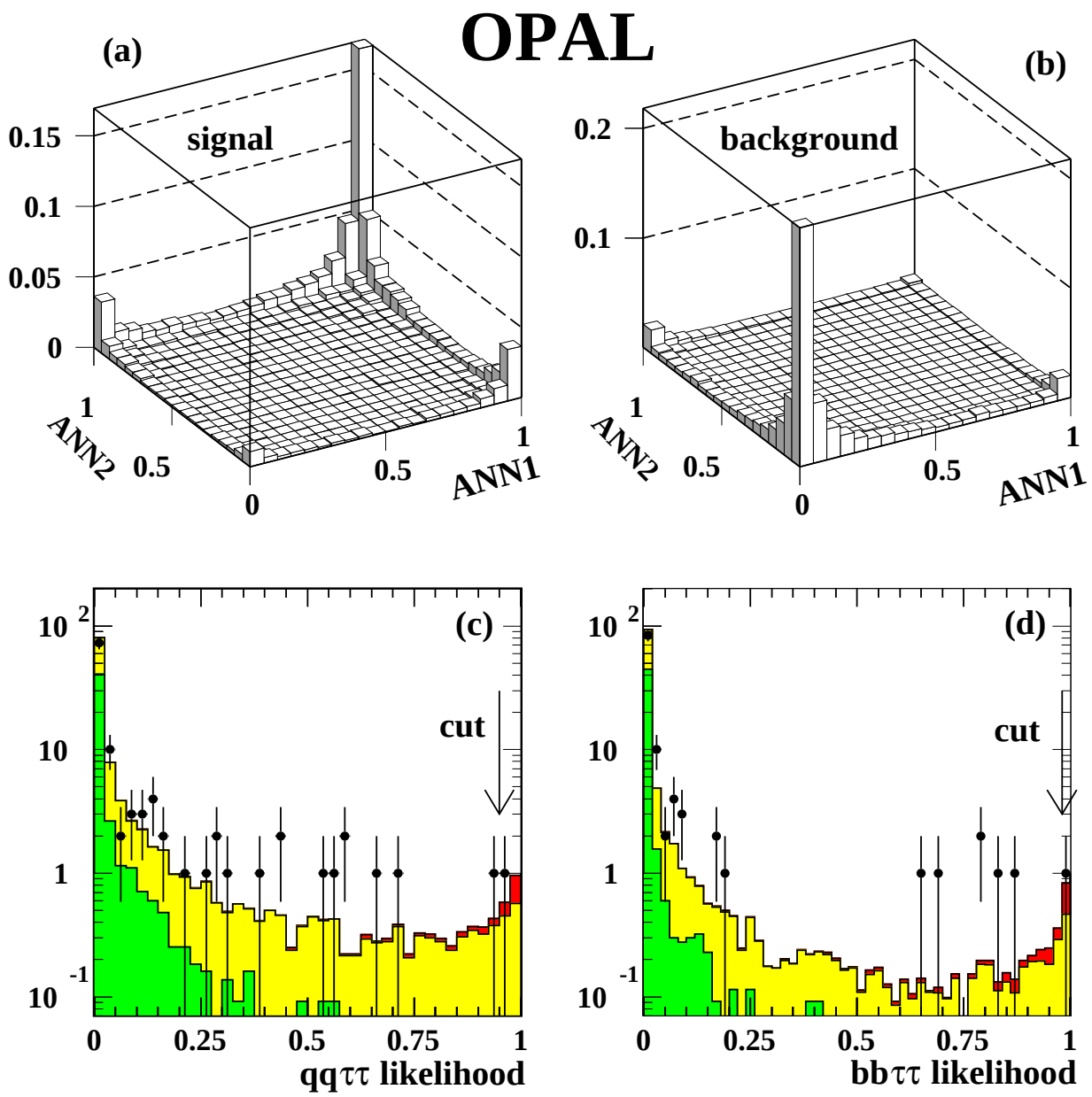

Figure 6: *Tau channel: the distributions of the two largest oppositely-charged tau ANN outputs for a Higgs* $q\bar{q}\tau^+\tau^-$ *signal* ($m_{H^0} = 85$ *GeV) (a) and the SM background (b). The distributions of* $\mathcal{L}(q\bar{q}\tau^+\tau^-)$ *(c) and* $\mathcal{L}(b\bar{b}\tau^+\tau^-)$ *(d) for two-fermion background (dark grey), four-fermion background (light grey), OPAL data (points), and a simulated* 85 *GeV Higgs signal added to the SM background (black).*

Cut	Data 183 GeV	Total bkg.	$q\bar{q}(\gamma)$	4f	Efficiency (%) $m_{H^0} = 85$ GeV	Like-sign R(obs/exp)
Presel.	1596	1582	1007	575	77.6	0.98 ± 0.03
$\mathcal{L}_{\tau\tau}$	393	359	92	267	69.0	1.09 ± 0.06
2-C fit	113	115	50	65	55.3	1.10 ± 0.10
$\mathcal{L}_{HZ}$	1	1.3 ± 0.1	0.1	1.2	33.0	-

Table 4: *The numbers of events sequentially surviving each cut as observed in the data compared with the total background expected from SM processes for the tau channel. The background estimates are normalised to 53.7* pb^{-1}*. The errors are statistical only. Also shown is the signal efficiency for an 85 GeV Higgs boson (column 6) and the ratio of the number of observed events to the number expected for events with a like-sign tau pair (column 7, see text for details).*

decay products while the energy is determined from the fit. The 2-C fit is required to yield a χ^2-probability larger than 10^{-5}. The numbers of observed events passing these cuts and the numbers expected from the SM background processes are given in Table 4. The remaining events are used as input to two likelihood selections.

Since roughly 50% of the $H^0Z^0 \to q\bar{q}\tau^+\tau^-$ final state includes b-flavoured hadrons, one of the likelihoods uses b-tagging information, $\mathcal{L}(b\bar{b}\tau^+\tau^-)$, while a second likelihood ignores this information, $\mathcal{L}(q\bar{q}\tau^+\tau^-)$. After removing all tracks and clusters associated with the two tau candidates, the event is forced into two jets using the Durham algorithm. A 3-C kinematic fit is performed which, in addition to energy and momentum conservation, constrains either the $q\bar{q}$ or the $\tau^+\tau^-$ system to the Z^0 mass. Both combinations are tried and the one yielding the larger fit probability is retained. This procedure correctly assigns the $q\bar{q}$ pair in 93% (75%) for a Higgs mass of 60 (80) GeV. The following variables are used as input to both likelihoods: R_{vis}, $|\cos\theta_{\mathrm{miss}}|$, $\mathcal{L}_{\tau\tau}$, the logarithm of y_{34} in the Durham scheme applied to the full event including the tau candidates, the energy of the most energetic identified electron or muon in the event, the angles between each tau candidate and the nearest jet ($\cos\theta_{\mathrm{nearest}}$), the opening angle between the most likely (largest P_i) tau candidate and the missing momentum vector, and the logarithm of the fit probability for the more likely 3-C fit combination. The $\mathcal{L}(b\bar{b}\tau^+\tau^-)$ likelihood uses in addition the output of the b-tagging algorithm described in Section 3. The weight factors have been set to $w_b = w_c = w_{uds} = 1$. An event is retained if $\mathcal{L}(b\bar{b}\tau^+\tau^-)$ exceeds 0.98 or $\mathcal{L}(q\bar{q}\tau^+\tau^-)$ exceeds 0.95. For a Higgs mass of 85 GeV, this selection has an efficiency of 33.0%. One event survives the likelihood cut compatible with the $Z^0(\to q\bar{q})H^0(\to\tau^+\tau^-)$ signal hypothesis, consistent with the $1.3 \pm 0.1(\mathrm{stat}) \pm 0.2(\mathrm{syst})$ events expected from SM background processes. The fitted mass of the $\tau^+\tau^-$ pair is 22.7 GeV.

A sample of like-sign tau pairs can be used to cross-check estimate for the dominant background in which at least one of the tau candidates is a hadronic fake candidate. The last column of Table 4 shows the ratio of the number of observed to the number of expected events for this like-sign comparison for the first three cuts. The systematic uncertainty on the tau identification efficiency was estimated to be 3% using the mixed event samples (as described above) at $\sqrt{s} = m_{Z^0}$. Further uncertainties on the signal efficiency arise from the modelling of the b-hadron decay multiplicity, 1%; the modelling of b-fragmentation, 1%; and detector modelling, 1%. Adding these in quadrature yields a total systematic error on the signal efficiency of 3% (relative). The additional error from Monte Carlo statistics is 2%. The total

systematic error on the surviving background is 15% (relative) not including the the Monte Carlo statistical error and is dominated by uncertainties in the detector modelling of the fake tau rates and of the variables used to construct the final likelihood.

An alternate selection also employs a likelihood technique, but without using b-tagging information. The identification of tau leptons is performed by considering different sets of input variables targeted to three different types of tau lepton candidate, one such type consisting of explicitly identified electrons and muons. Other input variables exploit kinematic differences of the ensemble of tracks and clusters not associated with the tau lepton candidate pair. The efficiency of this analysis for $m_{\mathrm{H^0}}$= 85 GeV is 32.1% with total expected background similar to that of the main analysis. No candidate events are observed in the data. Of the selected simulated signal events 60% are in common to both analyses. Of the background accepted by the main analysis approximately 20% is also accepted by the alternative analysis.

4.4 The Electron and Muon Channels

The $\ell^+\ell^-\mathrm{q\bar{q}}$ (ℓ = e or μ) final state arises mainly from the process $\mathrm{e^+e^-}\to\mathrm{Z^0H^0}\to\ell^+\ell^-\mathrm{q\bar{q}}$. They amount to approximately 6% of the Higgs boson production cross-section with a small contribution (3.4% (relative) for $m_{\mathrm{H^0}}$=85 GeV) from the $\mathrm{Z^0Z^0}$ fusion process $\mathrm{e^+e^-}\to\mathrm{e^+e^-H^0}\to\mathrm{e^+e^-q\bar{q}}$. The analysis concentrates on those final states proceeding through the first process which yield a clean experimental signature in the form of large visible energy, two energetic, isolated, oppositely-charged leptons of the same species reconstructing to the $\mathrm{Z^0}$ boson mass, and two energetic hadronic jets carrying b-flavour. The dominant backgrounds are $(\mathrm{Z}/\gamma)^*\to\mathrm{q\bar{q}}$ and four-fermion processes. The selection is divided into two stages, a preselection and a likelihood selection.

The preselection is similar to cuts (1) – (3) described in [7] and proceeds as follows. (1) The number of tracks must be at least six; y_{34} in the Durham scheme has to be larger than 10^{-4}; $|P^z_{\mathrm{vis}}| < (E_{\mathrm{vis}} - 0.5\sqrt{s})$ and $E_{\mathrm{vis}} > 0.6\sqrt{s}$ are required. (2) There must be at least one pair of oppositely charged, same flavour leptons (e or μ) as defined in [7]. (3) The rest of the event, excluding the candidate lepton pair, is reconstructed as two jets using the Durham algorithm; for the muon channel, a 4-C kinematic fit is required to yield a χ^2 probability larger than 10^{-5}. The invariant mass of the lepton pair should be larger than 40 GeV.

Next, a likelihood selection using the following input variables is applied: $R_{\mathrm{vis}} = E_{\mathrm{vis}}/\sqrt{s}$, $\log_{10}(y_{34})$ in the Durham scheme, the transverse momenta of the two leptons ordered by energy and calculated with respect to the nearest jet axis, and the invariant mass of the two leptons. For the electron channel, electron identification variables are used in addition to the previous five variables: $(E/p)_{\mathrm{norm}} \equiv [(E/p) - 1]/\sigma$ of the two electron candidates[3], and the normalised ionisation loss[4], $(dE/dx)_{\mathrm{norm}}$ of the two electron candidates. ¿From these variables the likelihood $\mathcal{K}$ is calculated as explained in [7].

The b-flavour requirement is taken into account by combining $\mathcal{K}$ and the b-tagging discrim-

[3] E and p are cluster energies and track momenta, and σ is the error associated to E/p obtained from the measurement errors of E and p.

[4] $(dE/dx)_{\mathrm{norm}} = [(dE/dx) - (dE/dx)_{\mathrm{nominal}}]/\sigma$ where (dE/dx) is the truncated ionisation loss in the jet chamber, $(dE/dx)_{\mathrm{nominal}}$ is the nominal truncated ionisation loss for an electron, and σ is the error of (dE/dx).

inant $\mathcal{B}_{2\mathrm{jet}}$ from the two hadronic jets:

$$\mathcal{B}_{2\mathrm{jet}} = \frac{w_\mathrm{b} \cdot p_\mathrm{b}^{(1)} \cdot p_\mathrm{b}^{(2)}}{w_\mathrm{b} \cdot p_\mathrm{b}^{(1)} \cdot p_\mathrm{b}^{(2)} + w_\mathrm{c} \cdot p_\mathrm{c}^{(1)} \cdot p_\mathrm{c}^{(2)} + w_\mathrm{uds} \cdot p_\mathrm{uds}^{(1)} \cdot p_\mathrm{uds}^{(2)}} \quad ,$$

where $p_\mathrm{q}^{(i)} = f_\mathrm{q}^{\tau} \cdot f_\mathrm{q}^{\ell} \cdot f_\mathrm{q}^{s}$ with q = b, c, uds (see Eq. 3). The weight factors have been set to $w_\mathrm{b} = 0.22$, $w_\mathrm{c} = 0.17$ and $w_\mathrm{uds} = 0.61$, corresponding to the branching fractions for Z^0 decays. This is motivated by the fact that the dominant background arises from $\mathrm{Z}^0\mathrm{Z}^{0*}$ production.

The signal likelihood is given by:

$$\mathcal{L} = \frac{\mathcal{K} \cdot \mathcal{B}_{2\mathrm{jet}}}{\mathcal{K} \cdot \mathcal{B}_{2\mathrm{jet}} + (1-\mathcal{K})(1-\mathcal{B}_{2\mathrm{jet}})}.$$

Candidate events are required to have a likelihood $\mathcal{L}$ >0.9 (0.4) for the electron (muon) channel. The different cut values are the result of an optimisation which maximises the sensitivity of the two channels separately. The signal selection efficiency for an 85 GeV Higgs boson is 57.9 % (62.7 %) for the electron (muon) channel.

Distributions of some variables used in the likelihood selection are shown in Figure 7.

Cut	Data		Total bkg.		$\mathrm{q\bar{q}}(\gamma)$		4f		Efficiency $m_{\mathrm{H}^0} = 85$ GeV	
	e	μ	e	μ	e	μ	e	μ	e (%)	μ (%)
(1)	2732		2987		2254		733		92.5	87.0
(2)	53	27	39.7	33.5	23.4	25.7	16.3	7.8	67.4	76.6
(3)	40	10	34.0	11.5	20.3	8.3	13.7	3.2	66.9	75.7
Likelihood	0	1	0.37	0.27	0.02	0.0	0.35	0.27	57.9	62.7

Table 5: *The numbers of events after each preselection cut and the likelihood cut for the data and the expected background in the electron and muon channels. Background estimates are normalised to* 53.7 pb^{-1}. *The last two columns show the detection efficiencies for the processes* $\mathrm{e^+e^-}\rightarrow$(*$\mathrm{e^+e^-}$ or $\mu^+\mu^-$*)H^0 *for an 85 GeV Higgs boson.*

The numbers of observed and expected events after each stage of the selection are given in Table 5, together with the detection efficiency for an 85 GeV Higgs boson. The selection retains one event in the muon channel. The total background expectation is 0.64±0.08(stat.)±0.20(syst.) events (0.37±0.07 events in the electron channel, 0.27±0.06 events in the muon channel). The candidate event has a di-lepton mass of 65.5±3.7 GeV. The Higgs mass, obtained from a 4-C kinematic fit, is 108.7±2.7 GeV for the candidate event.

The signal selection efficiencies as a function of the Higgs boson mass are given in Table 15. These are affected by the following systematic uncertainties for the electron (muon) channel: uncertainties in the lepton identification, 0.5% (0.4%); uncertainties in modelling the likelihood variables 0.8% (0.3%); tracking resolution in the b-tagging, 0.9% (0.9%). Taking these uncertainties as independent and adding them in quadrature results in a total systematic uncertainty of 1.3% (1.0%) (relative errors). The additional error from Monte Carlo statistics is 1.2% (1.0%).

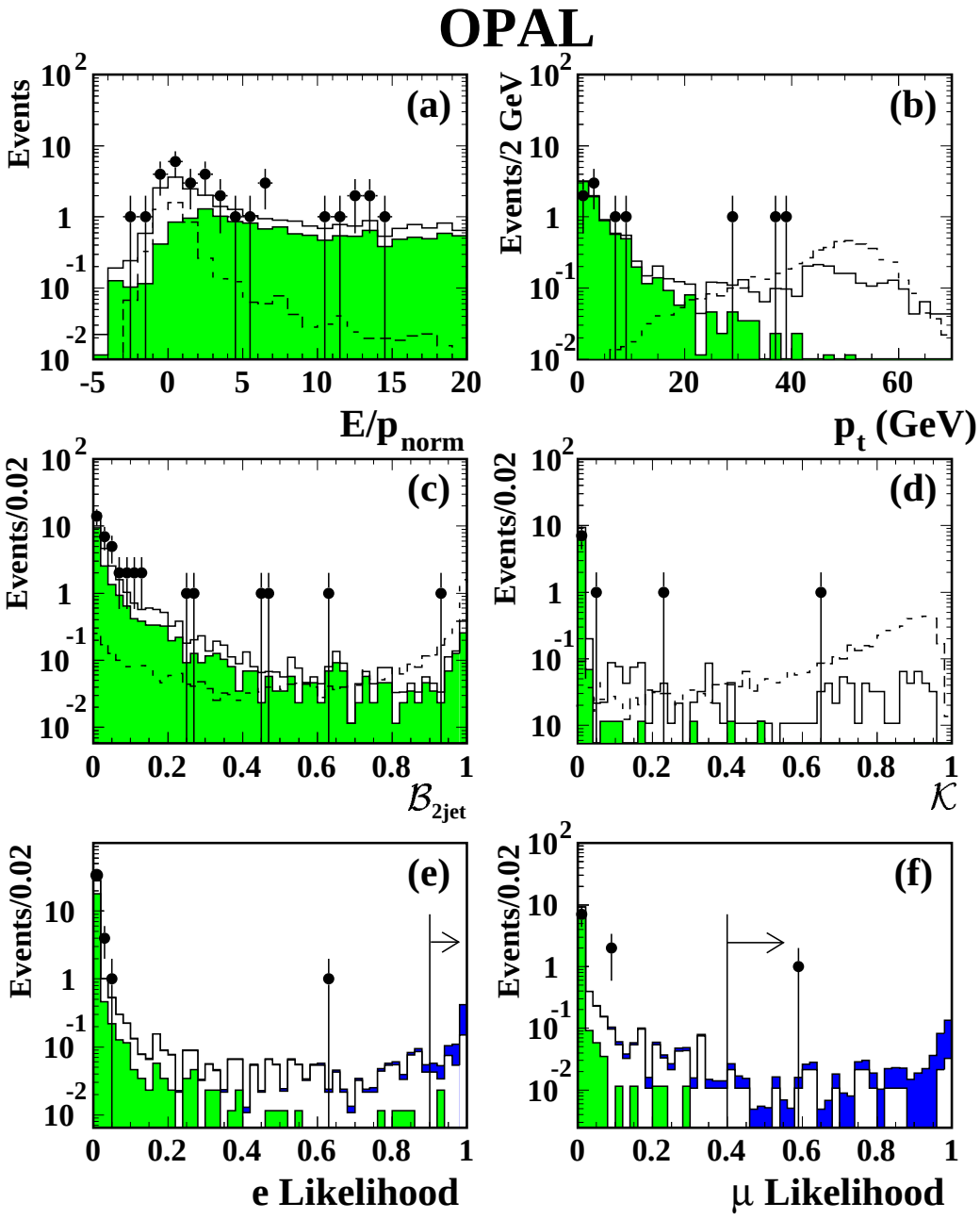

Figure 7: *Electron and muon channels: distributions used in the likelihood selection for pre-selected events: (a) $(E/p)_{\rm norm}$ for the higher energy electron candidate; (b) p_t of the higher momentum muon candidate; (c) $\mathcal{B}_{\rm 2jet}$ for the electron channel; (d) $\mathcal{K}$ for the muon channel; (e) final likelihood for the electron channel; (f) final likelihood for the muon channel. Data are shown as points with error bars. Background simulations, normalised to the integrated luminosity of 53.7* pb^{-1}*, are represented by the open (grey) histograms for four-fermion ($q\bar{q}$) events. Dashed lines show the expected signal distribution for an 85* GeV *Higgs boson. In (e) and (f), the signal simulation is added to the expected background (black area). The arrows indicate the position of the cuts. In (a)-(d) the simulated signal is scaled by a factor of 10 for better visibility.*

The residual background has the following systematic uncertainties: uncertainty in the lepton identification, 3.5%; uncertainties in modelling the likelihood variables, 7.5%; uncertainties in the generation of four-fermion processes, 25.2%; tracking resolution of 9.8%. The total systematic uncertainty on the background estimate is 28.3%. The additional error from Monte Carlo statistics is 12.5%.

4.5 Search for Z^0h^0 with $h^0 \to A^0A^0$

All of the above searches are also sensitive to the process $e^+e^- \to h^0Z^0$ followed by $h^0 \to A^0A^0$ and $A^0 \to b\bar{b}$ which appears in the 2HDM and the MSSM if kinematically allowed.

The selection in the four-jet channel described in Section 4.1 has been re-optimised for the $Z^0A^0A^0$ final state. The preselection cuts are kept, variables 3, 5 and 6 are dropped, and two variables sensitive to the six quark final state are added to the likelihood inputs: the logarithm of y_{56} in the Durham scheme and the number of good charged tracks in the event. Finally, the signal likelihood $\mathcal{L}^{HZ}$ is required to be larger than 0.98. The efficiency for $m_{h^0} = 60$ GeV and $m_{A^0} = 30$ GeV is 38.4±2.2(stat.)±3.1(syst.)%. The expected background is 1.8 events from $(Z/\gamma)^*$ and 2.6 events from four-fermion processes. Other sources of background are negligible. Four candidate events are selected, consistent with a total expected background of 4.4±0.3±0.9 events. Two of the candidate events selected in this analysis are the same as for the four-jet analysis of Section 4.1 (event 2 and event 6 in Table 2). The other two candidate events have reconstructed $m_{h^0}(\mathcal{L}^{HZ})$ of 59.5 GeV (0.999) and 77.9 GeV (0.983).

SM search	applied to the process	Efficiency (%)
four jet	$(A^0A^0 \to b\bar{b}b\bar{b})(Z^0 \to q\bar{q})$	38
missing energy	$(A^0A^0 \to b\bar{b}b\bar{b})(Z^0 \to \nu\bar{\nu})$	26
electron	$(A^0A^0 \to b\bar{b}b\bar{b})(Z^0 \to e^+e^-)$	75
muon	$(A^0A^0 \to b\bar{b}b\bar{b})(Z^0 \to \mu^+\mu^-)$	64
tau lepton	$(A^0A^0 \to b\bar{b}b\bar{b})(Z^0 \to \tau^+\tau^-)$	29

Table 6: *Signal detection efficiencies for the searches for the SM Higgs boson, applied to the processes with* $h^0 \to A^0A^0$ *followed by* $A^0 \to b\bar{b}$. *The efficiencies are quoted for* $m_{h^0} = 60$ *GeV and* $m_{A^0} = 30$ *GeV, with typical statistical errors of 1–4%.*

For the selections in the missing energy channel and the charged lepton channels, Monte Carlo simulations have demonstrated that the detection efficiencies for the two-stage process involving $h^0 \to A^0A^0$ followed by $A^0 \to b\bar{b}$ are close to those of the $h^0 \to b\bar{b}$ decay. For example, the detection efficiencies for $m_{h^0} = 60$ GeV and $m_{A^0} = 30$ GeV, a point close to the kinematical boundary of the process $h^0 \to A^0A^0$, are shown in Table 6. By construction, the candidate events selected are the same as for the corresponding $H^0 \to b\bar{b}$ analyses.

5 The A^0h^0 search channels

The process $e^+e^-\to A^0h^0$ which appears in the 2HDM and the MSSM is searched for in the final states $A^0h^0\to b\bar{b}b\bar{b}$ and $A^0h^0\to b\bar{b}\tau^+\tau^-$. The case $h^0\to A^0A^0$ as also treated in searching for the process $A^0h^0\to A^0A^0A^0\to b\bar{b}b\bar{b}b\bar{b}$.

5.1 The $A^0h^0\to b\bar{b}b\bar{b}$ Final State

The signature for events from the process $A^0h^0\to b\bar{b}b\bar{b}$ is four energetic jets containing b-hadron decays and a visible energy close to the centre-of-mass energy. The dominant background processes are $(Z/\gamma)^*\to q\bar{q}$, with or without initial state radiation accompanied by hard gluon radiation, and four-fermion processes, in particular hadronic W^+W^- final states. Z^0Z^{0*} production with both Z^0 bosons decaying into $b\bar{b}$ constitutes an irreducible background; however, its cross-section is small at a centre-of-mass energy of 183 GeV.

The event preselection proceeds through similar cuts as in the four jet channel described in Section 4.1; however, the cut value on the C–parameter (cut (4)) is 0.45. Cut (5) is replaced by the requirement that for each of the four jets, the sum of the reconstructed charged tracks and unassociated electromagnetic calorimeter clusters remaining after the energy-flow calculation [21] be larger than six. No 5-C fit is performed in cut (6).

For events passing the preselection, a likelihood technique is applied to classify the events as belonging to one of the three classes: $(Z/\gamma)^*$, four-fermion processes, or $A^0h^0\to b\bar{b}b\bar{b}$. Seven input variables are used. Four variables are the b-tagging discriminants $\mathcal{B}_i$ described in Section 3 (the index i denotes the jet number). In the calculation of $\mathcal{B}_i$, the weight factors have been optimised for this search, $w_b = w_c = 0.2$ and $w_{uds} = 0.6$. The four jets are ordered with decreasing jet energy. These variables are supplemented by y_{34} in the Durham scheme, the event thrust T, and the mean $|\cos\theta_{jet}|$ of the four jets.

The distributions of four of the seven input variables are shown in Figure 8. The final likelihood discriminant $\mathcal{L}^{Ah}$ is also shown.

Cut	Data 183 GeV	Total bkg.	$q\bar{q}(\gamma)$	4f	$\gamma\gamma$	Efficiency (%) $m_{A^0} = m_{h^0} = 70$ GeV
(1)	6131	6153	5096	950	108	99.8
(2)	1956	1959	1405	549	5.2	96.5
(3)	711	677	254	421	2.1	87.8
(4)	562	540	140	398	1.6	85.8
(5)	447	434	106	328	0.7	83.2
(6)	433	418	99	319	0.1	80.7
$\mathcal{L}^{Ah} > 0.95$	4	2.92±0.18	1.43	1.49	–	50.3

Table 7: *Effect of the cuts on data, background (normalised to the integrated luminosity of 54.1* pb^{-1}*) and signal simulation (m_{h^0}=m_{A^0}=70 GeV) for* $h^0A^0\to b\bar{b}b\bar{b}$. *The quoted error on the background is statistical.*

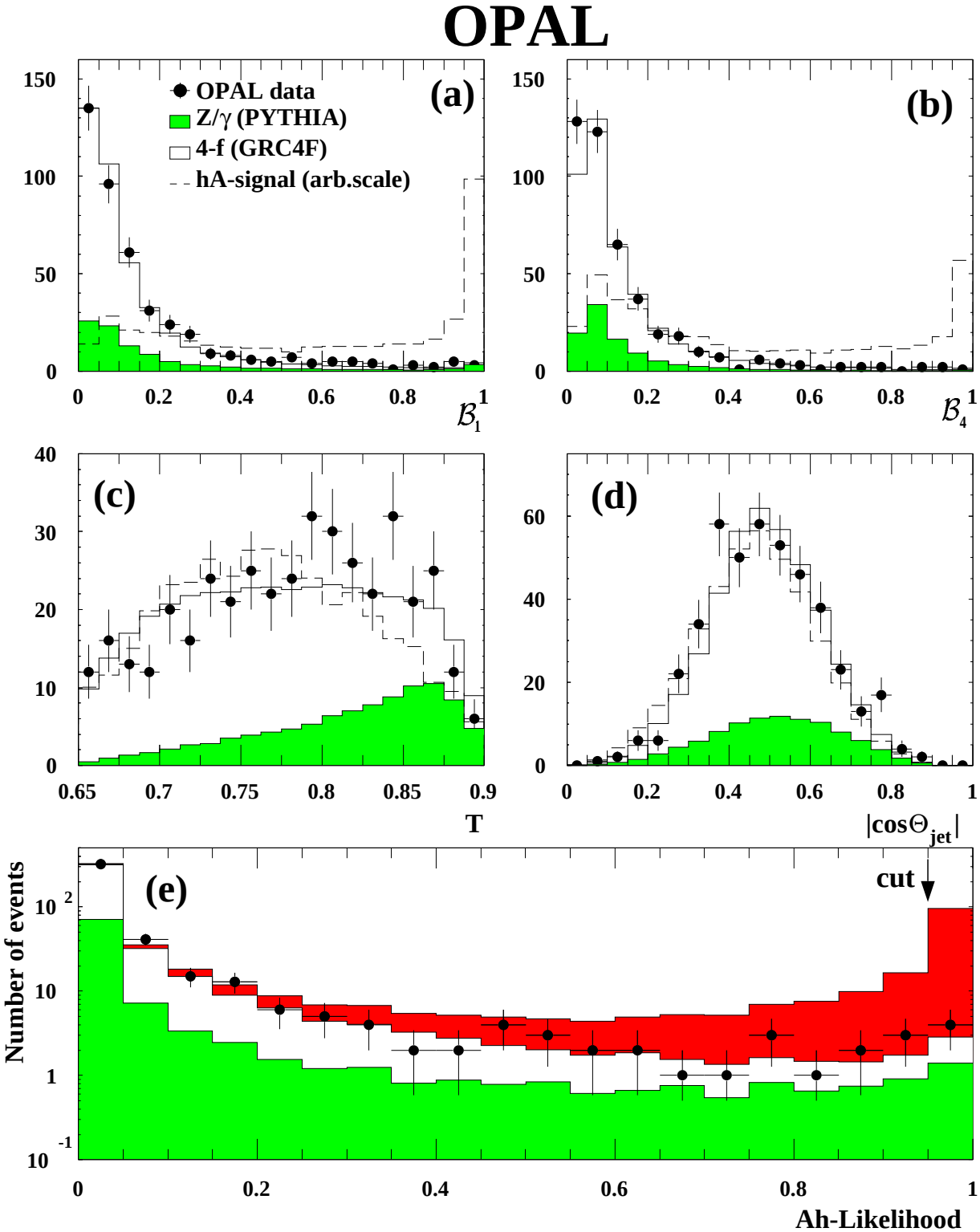

Figure 8: $A^0h^0 \to b\bar{b}b\bar{b}$-*channel: (a)–(d) distribution of input variables to the likelihood selection (as described in the text) for data compared to Monte Carlo expectations. (e) distribution of the likelihood output variable* $\mathcal{L}^{Ah}$*. The points with error bars are data, the shaded (open) histogram is the simulation of* $(Z/\gamma)^* \to q\bar{q}$ *(four-fermion) events, normalised to the recorded luminosity. The dashed line in (a)–(d) and the dark area in (e) represent a simulated signal* ($m_{h^0}=m_{A^0}=70$ *GeV) scaled arbitrarily for better visibility. The arrow in (e) indicates the position of the cut.*

Candidate events are selected by requiring $\mathcal{L}^{\mathrm{Ah}} > 0.95$. Four candidate events are observed in the data, consistent with 2.9±0.2(stat.)±0.5(syst.) events expected from SM background processes. Two of the four candidate events are common to those found in the four jet channel of Section 4.1, and one is in common with the $\mathrm{Z^0h^0}\to\mathrm{Z^0A^0A^0}\to\mathrm{q\bar{q}b\bar{b}b\bar{b}}$ search of Section 4.5.

Table 7 shows the number of selected events together with the expectation from background processes and the signal selection efficiency for $m_{\mathrm{A^0}} = m_{\mathrm{h^0}} = 70$ GeV, after each cut in the preselection and after the final cut on $\mathcal{L}^{\mathrm{Ah}}$.

Candidate	combination 1		combination 2		combination 3	
	m_1 (GeV)	m_2 (GeV)	m_1 (GeV)	m_2 (GeV)	m_1 (GeV)	m_2 (GeV)
1	34.2	141.3	32.4	71.3	41.9	75.5
2	25.1	114.0	43.3	99.3	36.3	87.0
3	30.4	70.1	69.4	106.2	78.1	87.6
4	34.3	83.3	68.8	110.5	70.7	86.0

Table 8: *Reconstructed di-jet mass combinations for the four candidate events in the search for* $\mathrm{A^0h^0}\to\mathrm{b\bar{b}b\bar{b}}$. *The last two events are also selected by the four jet selection.*

The systematic uncertainties on the signal selection efficiencies and background estimates were determined using the same methods as described in Section 4.1. The overall systematic uncertainty is 4% on the selection efficiencies and 17% on the expected number of background events.

Candidate Higgs masses are calculated from the measured jet momenta using a 4-C fit. Since the four jets can be combined in three ways, and since $\mathrm{h^0}$ and $\mathrm{A^0}$ cannot be distinguished, each candidate event enters at six points in the ($m_{\mathrm{A^0}}$,$m_{\mathrm{h^0}}$) plane. The resolution on the mass sum, $M = m_{\mathrm{A^0}} + m_{\mathrm{h^0}}$, is estimated to be approximately 3 GeV for $M = 150$ GeV [8]. For $m_{\mathrm{A^0}} = m_{\mathrm{h^0}}$, 68% of the events have a reconstructed mass difference $|m_{\mathrm{A^0}}{}^{\mathrm{rec}} - m_{\mathrm{h^0}}{}^{\mathrm{rec}}|$ of less than 13 GeV. The di-jet masses of the four candidate events are given in Table 8.

5.2 The $\mathrm{A^0h^0}\to\mathrm{b\bar{b}}\tau^+\tau^-$ Final State

The $\mathrm{A^0h^0}\to\mathrm{b\bar{b}}\tau^+\tau^-$final state, where either $\mathrm{A^0}$ or $\mathrm{h^0}$ decays into the tau pair, is topologically similar to the $\mathrm{H^0Z^0}\to\mathrm{q\bar{q}}\tau^+\tau^-$ final state described in Section 4.3, the main difference being the loss of the $\mathrm{Z^0}$ mass constraint. Therefore the selection proceeds in exactly the same manner as described in Section 4.3, with only a minor modification in the final likelihood selection. Here only the $\mathcal{L}(\mathrm{b\bar{b}}\tau^+\tau^-)$ likelihood is used, calculated without the 3-C fit probability and the opening angle between the most likely tau and the missing momentum vector. With a cut on this modified likelihood, ($\mathcal{L}_{\mathrm{hA}}$) at 0.9, an efficiency of 44.7±1.6(stat.)±1.8(syst.) % for $m_{\mathrm{h^0}} = m_{\mathrm{A^0}} = 70$ GeV is obtained. Three candidates are observed in the data, one of which is the $\mathrm{q\bar{q}}\tau^+\tau^-$candidate reported in Section 4.3. This is consistent with the 1.5±0.1(stat.)±0.2(syst.) events expected from SM background processes. The invariant masses $m_{\tau\tau}$ (m_{had}) of the three candidate events are 38.6 GeV (79.4 GeV), 20.6 GeV (94.1 GeV), and 84.9 GeV (46.0 GeV).

Since the A^0 and h^0 cannot be distinguished, each event enters two times in the (m_{A^0},m_{h^0}) plane. Systematic uncertainties on backgrounds and efficiencies were evaluated as in Section 4.3.

5.3 The $A^0h^0 \to A^0A^0A^0 \to b\bar{b}b\bar{b}b\bar{b}$ Final State

When $2m_{A^0} \leq m_{h^0}$, the decay $h^0 \to A^0A^0$ is kinematically allowed and may be the dominant decay in parts of the 2HDM and MSSM parameter space. In this case the process $e^+e^- \to h^0A^0 \to A^0A^0A^0$ can have a large branching ratio to the final state $b\bar{b}b\bar{b}b\bar{b}$. The events are characterised by a large number of jets and a large charged track multiplicity. To reduce backgrounds, b-tagging plays a crucial role. At 183 GeV, backgrounds from $(Z/\gamma)^* \to b\bar{b}g(\gamma)$ with hard gluon emission and four-fermion processes contribute approximately equally. Backgrounds from two-photon processes are reduced to a negligible level in the course of the event selection.

The selection is identical to that described in [8], consisting of five cuts: (1) requirement of a hadronic final state [35]; (2) at least five jets with $y_{\rm cut} = 0.0015$ using the Durham algorithm; (3) $\sqrt{s'} > 110$ GeV; (4) more than 35 charged particle tracks; (5) three or more jets with evidence for b flavour using the b-tagging algorithm described in [8]. Distributions of the variables relevant for the selection were compared with Monte Carlo simulations and found to agree reasonably well within the limited statistics of the data.

The numbers of events passing each requirement, compared with estimates from the background simulations, are shown in Table 9. Also shown are the detection efficiencies for a simulated signal sample with $m_{h^0} = 60$ GeV and $m_{A^0} = 30$ GeV. Two events pass the selection requirements, consistent with the background expectation of 2.3±0.2 events.

Cut	Data 183 GeV	Total bkg.	$q\bar{q}(\gamma)$	4f	Efficiency (%) $(m_{h^0}, m_{A^0}) = (60,30)$ GeV
(1)	6131	6047	5097	950	99.5
(2)	997	840	517	322	88.2
(3)	622	538	234	304	81.2
(4)	198	181	53	128	67.0
(5)	2	2.3±0.2	1.2	1.1	36.0

Table 9: *Effect of the selection criteria on data, background (normalised to the integrated luminosity of 54.1* $\rm pb^{-1}$*) and signal simulation ($m_{h^0} = 60$ GeV, $m_{A^0} = 30$ GeV) for the signal channel* $h^0A^0 \to b\bar{b}b\bar{b}b\bar{b}$*. The quoted error on the background is statistical.*

The systematic errors on the signal detection efficiencies (background estimates) are: jet reconstruction, 1.3% (4.3%); requirement on $\sqrt{s'}$, 1.3% (1.6%); tracking resolution, 0.8% (11.8%); uncertainty in the b-hadron decay multiplicity, 1.3%; mismodelling of detector effects on the multiplicity, 4.2% (9.6%). Different Monte Carlo generators to simulate the SM background processes (HERWIG instead of PYTHIA for $(Z/\gamma)^*$-events and EXCALIBUR instead of grc4f for four-fermion events) were found to be statistically consistent. The total systematic error on the detection efficiency (background estimate) is 4.8% (15.9%). The additional error from Monte Carlo statistics is 6% (7%).

An alternative search for $e^+e^- \to h^0A^0 \to A^0A^0A^0 \to b\bar{b}b\bar{b}b\bar{b}$ has also been performed. Selection of candidates is done through a neural network analysis which combines kinematic and topological variables with heavy flavour tagging. The sensitivity of this analysis is similar to the main analysis. For example, the efficiency of the ANN analysis (the main analysis) is 47.2% (41.6%) for $m_{h^0} = 60$ GeV and $m_{A^0} = 30$ GeV and 26.6% (28.2%) for $m_{h^0} = 70$ GeV and $m_{A^0} = 20$ GeV with similar background levels for the two analyses. Of the selected simulated signal events approximately 60% (depending on the masses) are in common to both analyses. Of the accepted background cross-section for the main analysis 20% is also accepted by the ANN analysis. One of the two selected candidate events of the ANN analysis is in common with the main analysis.

6 The $H^\pm$ search channels

In this search we consider leptonic and hadronic decays of charged Higgs bosons. The charged Higgs production process $e^+e^- \to H^+H^-$ is searched for in the three final states $H^+H^- \to \tau^+\nu_\tau\tau^-\bar{\nu}_\tau$ (leptonic final state), $H^+H^- \to \tau\nu_\tau q\overline{q}'$ (semileptonic final state), and $H^+H^- \to q\overline{q}'q\overline{q}'$ (hadronic final state).

6.1 The Leptonic Final State

A search at $\sqrt{s} = 161$, 172 and 183 GeV for pair-produced charged Higgs bosons in the leptonic channel, $H^+H^- \to \tau^+\nu_\tau\tau^-\bar{\nu}_\tau$, has been described in detail in [17] within the context of a general search for the anomalous production of di-lepton events with missing transverse momentum. A likelihood technique is employed to combine information from the various discriminating variables. A cut is made on the relative likelihood of an event being consistent with the charged Higgs signal hypothesis as opposed to the Standard Model background hypothesis. The cut value is adjusted such that the *a priori* average value of the 95% CL upper limit on the cross-section for H^+H^- is minimised using Monte Carlo simulation only. The optimisation is performed separately at each value of $\sqrt{s}$ and for each value of $m_{H^\pm}$ in 5 GeV steps.

The results of the analysis at 183 GeV are summarised in Table 10. The numbers of selected candidates are in agreement with the Standard Model expectation. The dominant Standard Model background results from W^+W^- production, which is well understood and for which the available high statistics Monte Carlo samples describe well the OPAL data [41]. The systematic error on the expected background was estimated to be 5%. In addition to the uncertainty due to the limited Monte Carlo statistics for H^+H^-, the systematic error on the selection efficiency was estimated to be 5% taking into account deficiencies in the Monte Carlo generators and the detector simulation.

6.2 The Semileptonic Final State

The semileptonic channel $H^+H^- \to \tau^+\nu_\tau q\overline{q}'$ (or the charge-conjugate decay) is characterised by an isolated tau lepton, a pair of acoplanar jets and sizable missing energy and momentum. The

Selection for $m_{\mathrm{H}^{\pm}}$ (GeV)	Data 183 GeV	Exp. background	Efficiency (%)
50	4	6.58±0.31	38.9
60	5	7.48±0.32	42.9
70	5	9.17±0.36	48.6
80	8	9.65±0.36	51.4
90	4	6.35±0.27	45.1

Table 10: *Leptonic charged Higgs channel: the number of selected and expected events together with selection efficiencies at $\sqrt{s} = 183$ GeV for different values of $m_{\mathrm{H}^{\pm}}$. Monte Carlo statistical errors are given. Note that there is significant overlap between the various $m_{\mathrm{H}^{\pm}}$-dependent selections. The background expectations are normalised to the integrated luminosity of 55.8* pb^{-1}.

main background comes from the $\mathrm{W}^+\mathrm{W}^- \to \mathrm{q}\overline{\mathrm{q}}'\ell^+\nu_\ell$ process which has a similar topology to the signal, particularly if the charged Higgs boson mass is close to the $\mathrm{W}^{\pm}$ mass.

The analysis proceeds in two steps. First, events consistent with the final state topology are preselected. These events are then categorised into different classes using a likelihood method.

The preselection consists of the following cuts: (1) the event must qualify as a hadronic final state [35] with (2) significant missing energy, $R_{\mathrm{vis}} = E_{\mathrm{vis}}/\sqrt{s} < 0.85$. (3) The total missing momentum transverse to the beam direction (P^T_{vis}) has to be larger than 10 GeV. The polar angle of the missing momentum is required to satisfy $|\cos\theta_{\mathrm{miss}}| < 0.9$. The sum of the energies in the forward detector, gamma catcher and silicon tungsten calorimeter is required to be less than 20 GeV. (4) There must be at least one tau lepton identified by the track-based ANN algorithm, described in Section 4.3, with output larger than 0.5. If there is more than one tau lepton candidate in the event, the one with the largest ANN output is retained. (5) The two hadronic jets of the event are defined using the Durham algorithm after removing the decay products of the tau lepton. Both jets should contain at least one charged track.

The likelihood selection uses 12 input variables to further exploit the differences between the signal and the background events. Three event classes are defined: two-fermion events, four-fermion events, and $\mathrm{H}^+\mathrm{H}^- \to \tau^+\nu_\tau \mathrm{q}\overline{\mathrm{q}}'$. The input variables are: the transverse momentum of the event (p_T), the scalar sum of the charged track momenta (Σp), the number of charged tracks in a 30° cone around the tau direction excluding the tracks within the 10° tau cone the cosine of the angle between the tau and the nearest jet, ($\cos\theta_{\mathrm{nearest}}$), the tau lepton ANN output, the number of charged tracks within the tau cone (N^{CT}_τ), the highest track momentum (p_{max}), the highest electromagnetic cluster energy (E_{max}), the polar angle of the hadronic system multiplied by the sign of the tau lepton charge ($Q_\tau \cos\theta_{\mathrm{hadr}}$), the polar angle of the tau lepton in the rest-frame of the hadronic system multiplied by the sign of the tau lepton charge ($Q_\tau \cos\theta^*_\tau$), the C-parameter, and the Durham scheme jet resolution parameter y^{hadr}_{12}, calculated from the hadronic system after removing the tau lepton candidate.

Candidate events are selected if their likelihood output $\mathcal{L}$ is greater than 0.85.

In Figure 9, the distributions of six likelihood input variables are shown. The resulting likelihood distributions are shown in Figure 10(a).

Table 11 shows the number of selected data events at 183 GeV, the expected background

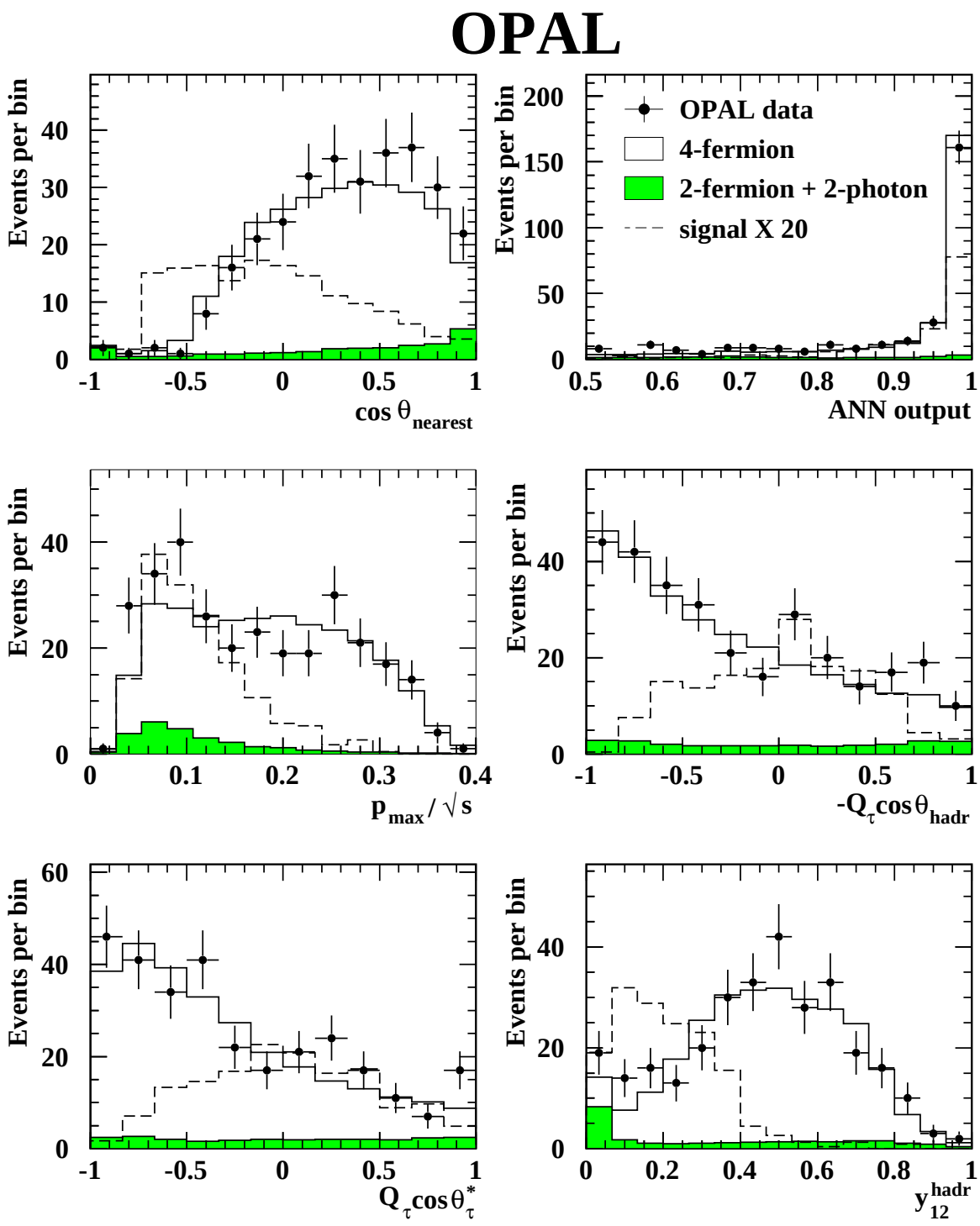

Figure 9: *Semileptonic charged Higgs boson channel: distributions used in the likelihood selection (see text for explanation). The points with error bars are data, the shaded (open) histogram is the simulation of two-fermion (four-fermion) events, normalised to the recorded luminosity. The dashed line is a simulated signal ($m_{\mathrm{H}^{\pm}} = 60$ GeV) assuming BR($\mathrm{H}^{+} \to \tau^{+}\nu_{\tau}$) = 0.5 and scaled by a factor of 20 for better visibility.*

and the signal efficiency for $m_{\mathrm{H}^\pm} = 60$ GeV after each cut. After all requirements, 16 events are selected in the data sample, while 15.3±0.4(stat.)±1.8(syst.) events are expected from Standard Model processes. Of these, the four-fermion processes account for 98%.

Cut	Data 183 GeV	Total bkg.	$\mathrm{q\bar{q}}(\gamma)$	4f	$\gamma\gamma$	Efficiency (%) $m_{\mathrm{H}^\pm} = 60$ GeV
(1)	6333	6405	5304	987	114	94.4
(2)	3642	3466	2889	502	75.1	89.8
(3)	536	478	158	320	0.8	85.2
(4)	304	285	29.2	256	0.8	71.0
(5)	298	279	24.8	253	0.8	69.6
$\mathcal{L} > 0.85$	16	15.3±0.4	0.3±0.1	15.0±0.4	—	48.6±2.2

Table 11: *Semileptonic charged Higgs boson channel: comparison of the number of observed events and expected background (normalised to 56.2* pb^{-1}*) together with the selected fraction of simulated signal events ($m_{\mathrm{H}^\pm} = 60$ GeV) after each cut. The errors are statistical.*

The signal detection efficiencies are listed in Table 12. A decrease of the efficiency is observed with increasing Higgs mass, since the signal topology becomes more and more background-like. In the calculation of the efficiencies and backgrounds a reduction by 1.8% (relative) has been applied in order to account for accidental vetos due to accelerator-related backgrounds in the forward detectors.

Signal selection efficiencies (%)								
50 GeV	55 GeV	60 GeV	65 GeV	70 GeV	75 GeV	80 GeV	85 GeV	90 GeV
47.8±2.2	50.4±2.2	48.6±2.2	46.4±2.2	35.0±2.1	30.6±2.1	17.4±1.7	7.0±1.1	3.2±0.8

Table 12: *Semileptonic charged Higgs boson channel: signal selection efficiencies (in %) for various charged Higgs masses. The errors are statistical.*

The Higgs mass is reconstructed from the hadronic system with 2.0 – 2.5 GeV resolution using a one-constraint kinematic fit requiring energy and momentum conservation and the decay of two equal mass objects. If the fit has a χ^2 probability of less than 10^{-5}, the mass is calculated, instead, from the measured jet four-momenta using the angular information and scaling the total energy of the hadronic system to the beam energy. The resulting mass distributions are shown in Figure 10(b).

The signal selection efficiencies are affected by systematic uncertainties on the tau lepton identification (3.0%) and the modelling of the kinematic variables (4.8%). The total systematic uncertainty is 5.7%. The additional statistical error of the background Monte Carlo samples is 2.5%. The background estimate is affected by the following systematic uncertainties: modelling of the hadronisation process estimated by comparing different event generators (8%), uncertainty on the tau lepton identification (3%), and modelling of the kinematic variables (9%). The total systematic error on the background estimate is 12%. The additional error from Monte Carlo statistics is typically 5%.

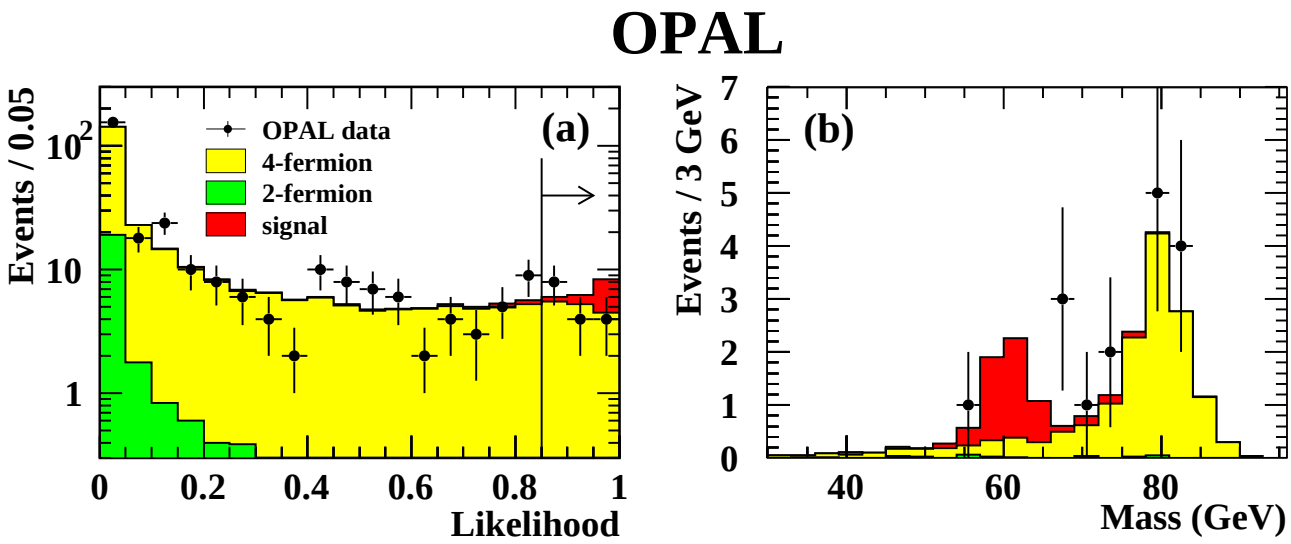

Figure 10: *Semileptonic charged Higgs boson channel: (a) the likelihood output and (b) the invariant mass distribution for 183 GeV data. The points with error bars are data, the grey (light grey) histogram is the simulation of two-fermion (four-fermion) events, normalised to the recorded luminosity. The dark grey histogram is a simulated signal ($m_{\mathrm{H}^{\pm}} = 60$ GeV) assuming BR($\mathrm{H}^+ \to \tau^+\nu_\tau$) = 0.5 added to the background expectation. The arrow indicates the cut on the likelihood output.*

6.3 The Hadronic Final State

The hadronic channel, $\mathrm{H}^+\mathrm{H}^- \to \mathrm{q}\overline{\mathrm{q}}'\mathrm{q}\overline{\mathrm{q}}'$, is characterised by an event topology of four well separated hadron jets and large visible energy. The background comes from $\mathrm{q}\bar{\mathrm{q}}(\gamma)$ events with hard gluon emission and from four-fermion processes, predominantly $\mathrm{W}^+\mathrm{W}^- \to \mathrm{q}\overline{\mathrm{q}}'\mathrm{q}\overline{\mathrm{q}}'$.

First, well-defined four-jet events are preselected; then a set of variables are combined using a likelihood technique.

The preselection consists of the following cuts: (1) The event must qualify as a hadronic final state [35]. (2) The effective centre-of-mass energy [35] ($\sqrt{s'}$) is required to be at least 150 GeV and the visible energy (E_{vis}) is required to be at least $0.7\sqrt{s}$. (3) The events are reconstructed into four jets using the Durham algorithm. The jet resolution parameter y_{34} has to be larger than 0.0025. Each jet must contain at least one charged track. (4) A 4-C fit requiring energy and momentum conservation is required to yield a χ^2 probability larger than 10^{-5}, and a 5-C fit requiring equal di-jet invariant masses in addition is required to converge and yield a χ^2 probability larger than 10^{-5} for at least one of the three jet pair combinations. (5) The C-parameter must be larger than 0.45.

To separate the signal from the background events surviving the preselection, a likelihood technique is applied. Three event classes are defined: two-fermion, four-fermion, and $\mathrm{H}^+\mathrm{H}^- \to \mathrm{q}\overline{\mathrm{q}}'\mathrm{q}\overline{\mathrm{q}}'$. The following five variables are used as input: the cosine of the smallest jet-jet angle ($\cos\alpha_{\mathrm{min}}$); the difference between the largest and smallest jet energy ($E_{\mathrm{max}} - E_{\mathrm{min}}$) after the 4-C fit; the cosine of the polar angle of the thrust axis ($\cos\theta_{\mathrm{thrust}}$); the cosine of the di-jet

Cut	Data 183 GeV	Total bkg.	$q\bar{q}(\gamma)$	4f	$\gamma\gamma$	Efficiency (%) $m_{H^\pm} = 60$ GeV
(1)	6333	6405	5304	987	114	100.
(2)	1939	1980	1457	519	4.3	97.0
(3)	707	703	280	422	1.3	89.0
(4)	534	542	183	358	0.4	78.0
(5)	454	445	104	341	0.3	76.6
$\mathcal{L} > 0.6$	50	48.8±0.7	9.0±0.3	39.8±0.7	—	42.8±2.2

Table 13: *Hadronic charged Higgs boson channel: Comparison of the number of observed events and expected background (normalised to 56.2* pb^{-1}*) together with the signal efficiency for* $m_{H^\pm} = 60$ *GeV after each cut. The errors are statistical.*

production angle ($\cos\theta_{\mathrm{di-jet}}$) multiplied by the di-jet charge[5] ($Q_{\mathrm{di-jet}}$) for the combination with the highest probability given by the 5-C fit; and the smallest di-jet mass difference (ΔM_{min}) after the 4-C fit. An event is selected if its likelihood output $\mathcal{L}$ is greater than 0.6.

Signal selection efficiencies (%)								
50 GeV	55 GeV	60 GeV	65 GeV	70 GeV	75 GeV	80 GeV	85 GeV	90 GeV
36.8±2.2	42.0±2.2	42.8±2.2	33.0±2.1	26.0±2.0	16.4±1.7	12.4±1.5	12.2±1.5	11.6±1.4

Table 14: *Hadronic charged Higgs boson channel: Signal selection efficiencies (in %) for various charged Higgs masses. The errors are statistical.*

In Figure 11 the distributions of the input variables to the likelihood selection are shown. The likelihood distribution is shown in Figure 12(a). Table 13 shows the number of selected events, the estimated background, and the fraction of signal events retained for $m_{H^\pm} = 60$ GeV after each cut. In total, 50 events are selected in the data, while 48.8±0.7 (statistical error) events are expected from Standard Model processes. The four-fermion processes account for 82% of the expected background, and result in a large peak centred at the $W^\pm$ mass.

For the selected events, the jet pair association giving the highest χ^2 probability in the 5-C fit is retained. The resulting mass resolution ranges from 1.0 GeV to 1.5 GeV. Figure 12(b) shows the invariant mass distribution of the selected events together with the Standard Model background expectation and a simulated signal of $m_{H^\pm} = 60$ GeV.

The uncertainties on the signal selection efficiency include typically 6% from the limited Monte Carlo statistics and 3% systematic uncertainty from the modelling of the cut variables.

Systematic uncertainties arise from modelling of the hadronisation process (2.0%), estimated by comparing different event generators and from modelling of the cut variables (4.9%), yielding a total systematic uncertainty of 5.3%. The additional error from Monte Carlo statistics is 1.6%.

[5]If there is more than one charged track in a jet, its charge is calculated as $\Sigma q^{(i)}\sqrt{p_{\mathrm{L}}^{(i)}}/\Sigma\sqrt{p_{\mathrm{L}}^{(i)}}$, where the sum goes over each track within the jet, $q^{(i)}$ is the charge of the track and $p_{\mathrm{L}}^{(i)}$ is its momentum parallel to the jet direction. A charge of +1 is assigned to the di-jet system with the larger sum of the two individual jet charges, and a charge of -1 to the other.

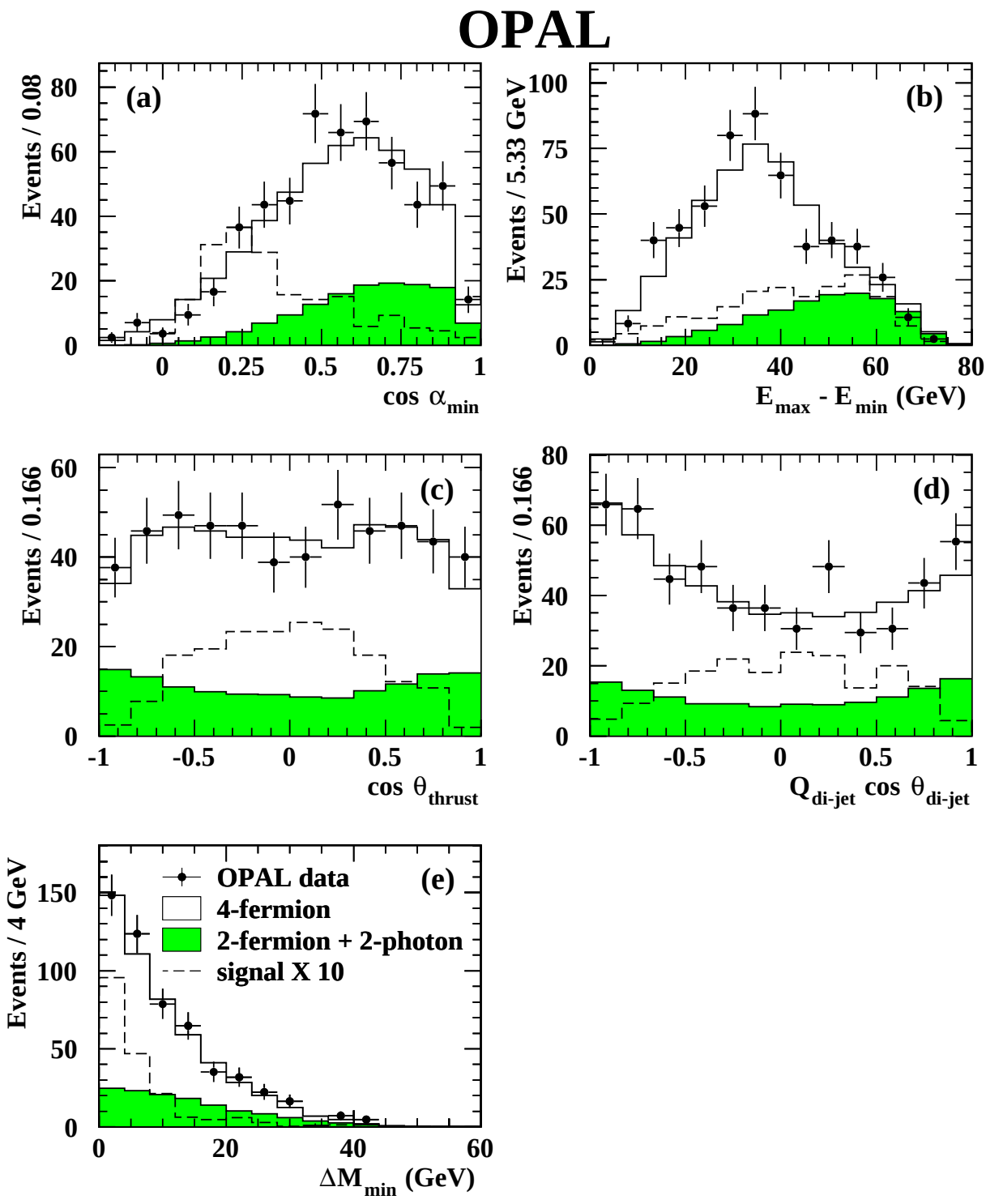

Figure 11: *Hadronic charged Higgs boson channel: distributions used in the likelihood selection. The points with error bars are data, the shaded (open) histogram is the simulation of two-fermion (four-fermion) events, normalised to the recorded luminosity. The dashed line is a simulated signal ($m_{\mathrm{H}^{\pm}}$ = 60 GeV) assuming BR($\mathrm{H}^{+}\mathrm{q}\overline{\mathrm{q}}'$) = 1 and scaled by a factor of 10 for better visibility.*

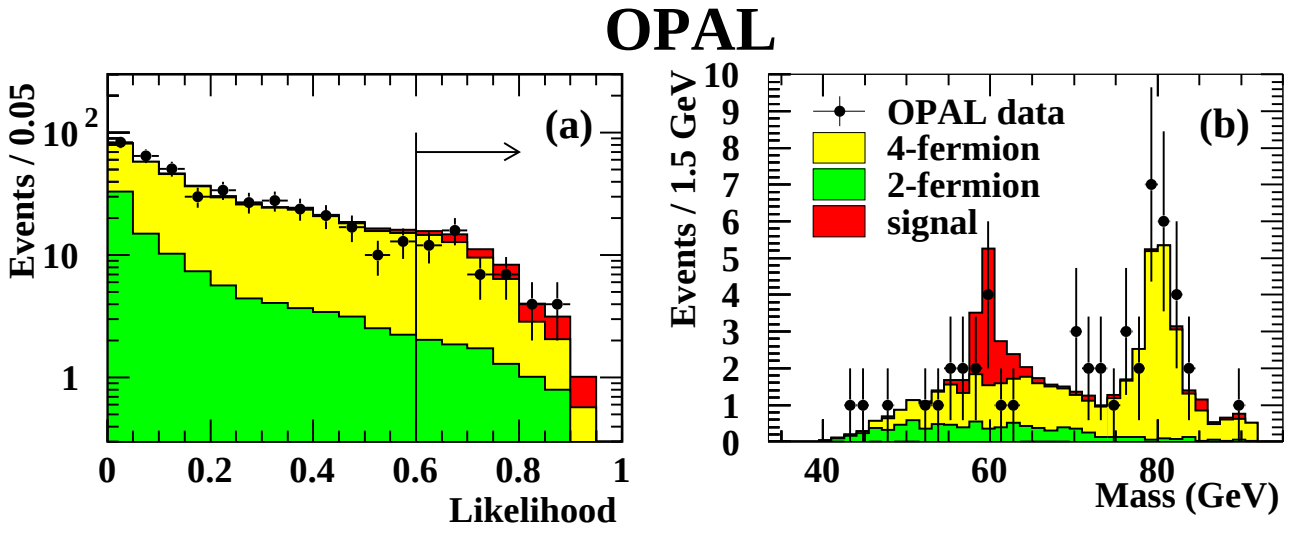

Figure 12: *Hadronic charged Higgs boson channel: (a) the likelihood output and (b) the invariant mass distribution. The points with error bars are data, the grey (light grey) histogram is the simulation of two-fermion (four-fermion) events, normalised to the recorded luminosity. The dark grey histogram is a simulated signal ($m_{\mathrm{H}^\pm}$ = 60 GeV) assuming BR($\mathrm{H}^+ \to \mathrm{q}\overline{\mathrm{q}}'$) = 1 added to the background expectation. The arrow indicates the cut on the likelihood output.*

7 Interpretation of the Search Results

None of the searches presented in the previous sections revealed a significant excess over the expectation from SM background processes. This negative result is used to derive limits at the 95% confidence level (CL) on neutral Higgs boson masses in the SM, in 2HDM and in the MSSM under various assumptions for the values of the free parameters of the models. A limit on the charged Higgs boson mass is also given.

The search channels are combined using the method described in Section 5 of [8]. This method takes into account the experimental mass resolution, including tails, in all search channels. The expected background is reduced by its systematic error in each channel and then subtracted.

7.1 Mass Limit for the Standard Model Higgs Boson

Table 15 lists the efficiencies and expected signal event rates for all search channels relevant for the SM Higgs boson as a function of the Higgs boson mass. The total expected event rate from all channels combined is also shown. In Figure 13 the masses of the nine candidate events are shown together with the expected background and a simulated signal at m_{H^0} = 85 GeV. Only the data taken at $\sqrt{s}$ ≈183 GeV are considered.

Figures 14 and 15 show the results for signal event rates and confidence levels for the signal and background hypotheses. At 95% CL the derived observed lower limit for the SM Higgs boson mass is found to be $m_{\mathrm{H}^0} > 88.3$ GeV, while the average expected limit from simulated background-only experiments is $m_{\mathrm{H}^0} > 86.1$ GeV. From Figure 15(b) it can be seen that this

m_{H^0} (GeV)	$q\bar{q}H^0$ $H^0 \to b\bar{b}$	$\nu\bar{\nu}H^0$	$\tau^+\tau^- q\bar{q}$	$e^+e^-H^0$	$\mu^+\mu^-H^0$	expected events (total)
70	30.2 (8.1)	41.7 (3.9)	31.2 (1.2)	57.3 (0.9)	69.0 (0.9)	15.0
75	33.9 (7.5)	43.8 (3.4)	32.5 (1.1)	58.5 (0.8)	60.7 (0.8)	13.5
80	37.1 (6.4)	43.7 (2.7)	33.1 (0.9)	58.7 (0.6)	62.0 (0.6)	11.2
85	39.2 (4.7)	40.2 (1.7)	33.0 (0.6)	57.9 (0.4)	62.7 (0.5)	7.9
90	39.4 (2.1)	34.6 (0.7)	32.0 (0.3)	55.2 (0.2)	62.1 (0.2)	3.4
95	36.6 (0.30)	28.7 (0.13)	29.9 (0.04)	47.0 (0.03)	57.7 (0.03)	0.53
100	29.9 (0.10)	26.4 (0.07)	26.6 (0.01)	32.3 (0.01)	47.2 (0.01)	0.20
Background	5.0±0.2	1.6±0.1	1.3±0.1	0.6±0.1		8.5±0.4
Systematics	±0.6	±0.2	±0.2	±0.1		± 0.7
Observed	7	0	1	1		9

Table 15: *Detection efficiencies (in %) and numbers of expected Higgs boson events (in parentheses) at* $\sqrt{s}$*= 183* GeV *for each search channel separately, as a function of the Higgs boson mass. The last column shows the total numbers of expected events in the present search at* $\sqrt{s}$*= 183* GeV .

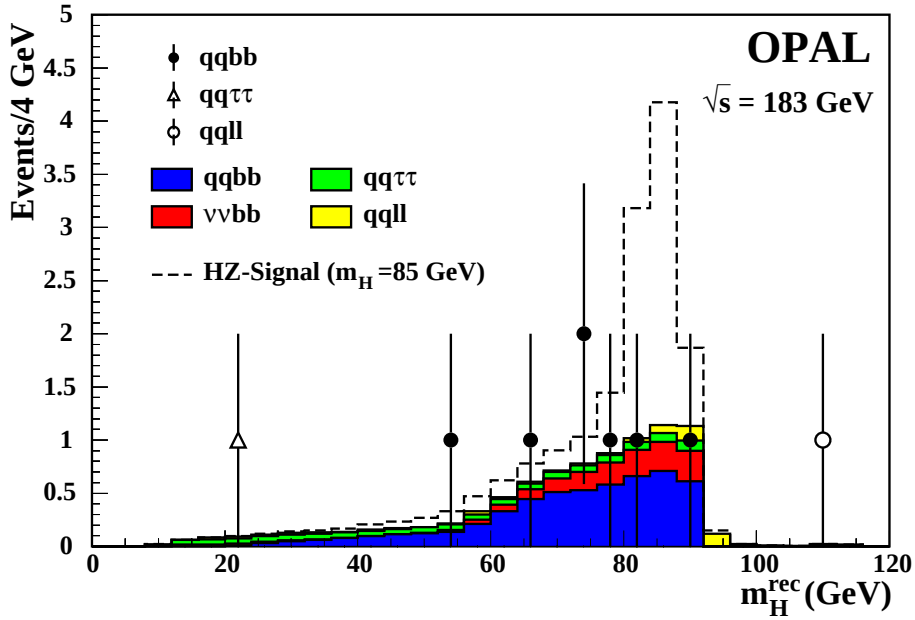

Figure 13: *Distribution of the reconstructed Higgs boson candidate masses,* m_H^{rec}*, for all SM channels. The data (points with error bars) are compared to the Monte Carlo expectations for the backgrounds from the various processes for the different selection channels (full histograms). A simulated signal for* m_{H^0} *= 85 GeV (dashed line) is also shown, added to the background expectation.*

observation is quite compatible with the SM background for Higgs boson mass hypotheses between 70 and 90 GeV. The probability for obtaining a limit larger than 88.3 GeV was found to be 40% if no signal is present.

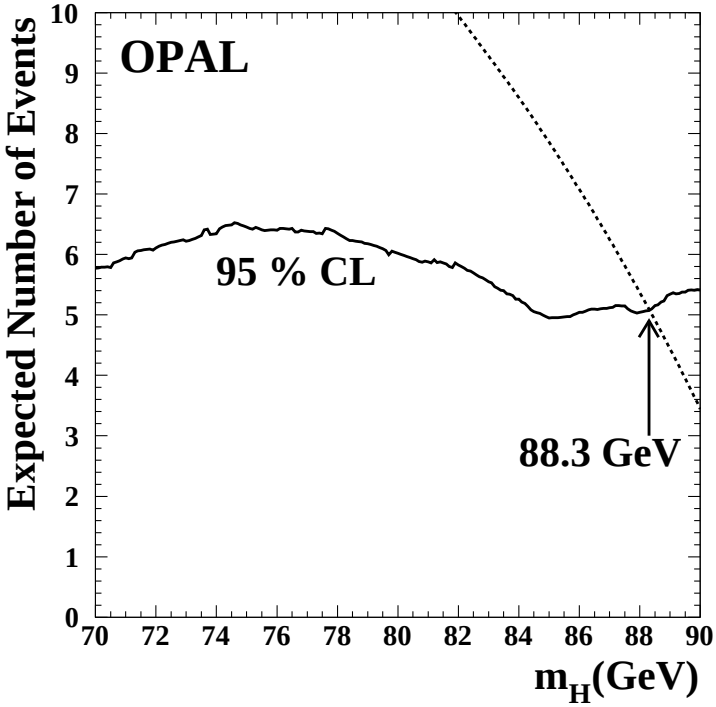

Figure 14: *Upper limit on the production rate for SM Higgs bosons at 95% CL (solid line) and the expected event rate (dashed line) as a function of the Higgs boson mass.*

7.2 Model–independent and 2HDM Interpretation

Model-independent limits are determined for the cross-section for the generic processes $e^+e^- \to S^0Z^0$ and $e^+e^- \to S^0P^0$, where S^0 and P^0 denote scalar and pseudo-scalar neutral bosons which decay into a pair of leptons or quarks, respectively. This is achieved by combining the searches presented in this publication with previous OPAL Higgs searches [7, 8, 42, 43] at $\sqrt{s}$ values between m_{Z^0} and 172 GeV. The limits are conveniently expressed in terms of scale factors, s^2 and c^2, which relate the cross-sections of these generic processes to those of the SM cross-sections (c.f. Eqs. (1), (2)):

$$\sigma_{SZ} = s^2 \; \sigma^{SM}_{HZ}, \tag{4}$$

$$\sigma_{SP} = c^2 \; \bar{\lambda} \; \sigma^{SM}_{\nu\bar{\nu}}. \tag{5}$$

Figure 16 shows the 95% CL upper bound for s^2 as a function of the S^0 mass, obtained using:

$$s^2 = \frac{N^{SZ}_{95}}{\sum \; (\epsilon \; \mathcal{L} \; \sigma^{SM}_{HZ})},$$

where N^{SZ}_{95} is the 95% CL upper limit for the number of possible signal events in the data, ϵ is the signal detection efficiency, $\mathcal{L}$ is the integrated luminosity, and the sum runs over the different centre-of-mass energies of the data. The solid line is computed using all SM search

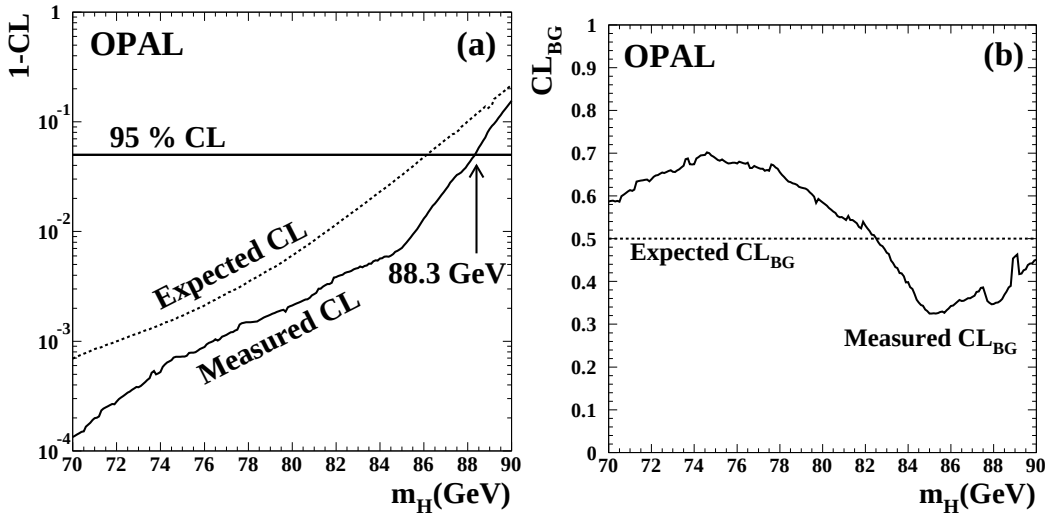

Figure 15: *Search for the SM Higgs boson: (a) Measured (solid line) and average expected (dashed line) confidence levels for the signal hypothesis as a function of the Higgs boson mass. (b) Measured (solid line) and average expected (dashed line) confidence levels for the background hypothesis as a function of the Higgs boson mass.*

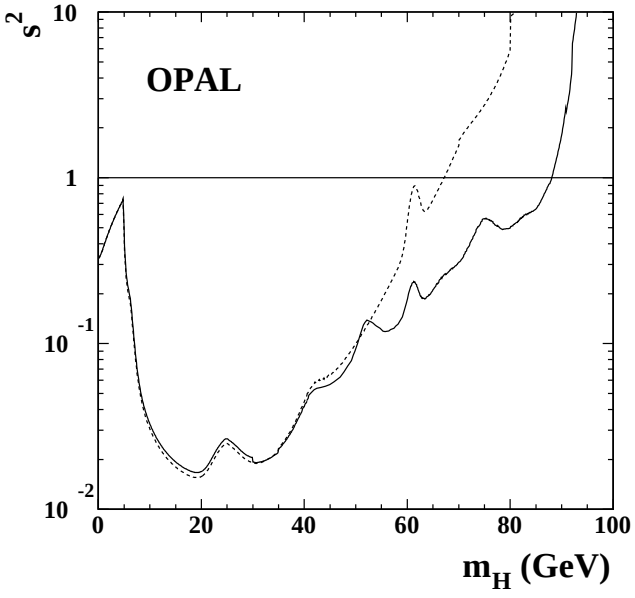

Figure 16: *Upper limits at 95% CL on s^2 (as defined by Eq. (4)) using all SM search channels and assuming the SM Higgs boson branching ratios for the S^0 (solid line). The dashed line is from a previous OPAL search [8] and includes only channels that do not use b-tagging. A hadronic branching ratio of the S^0 of 100% is assumed.*

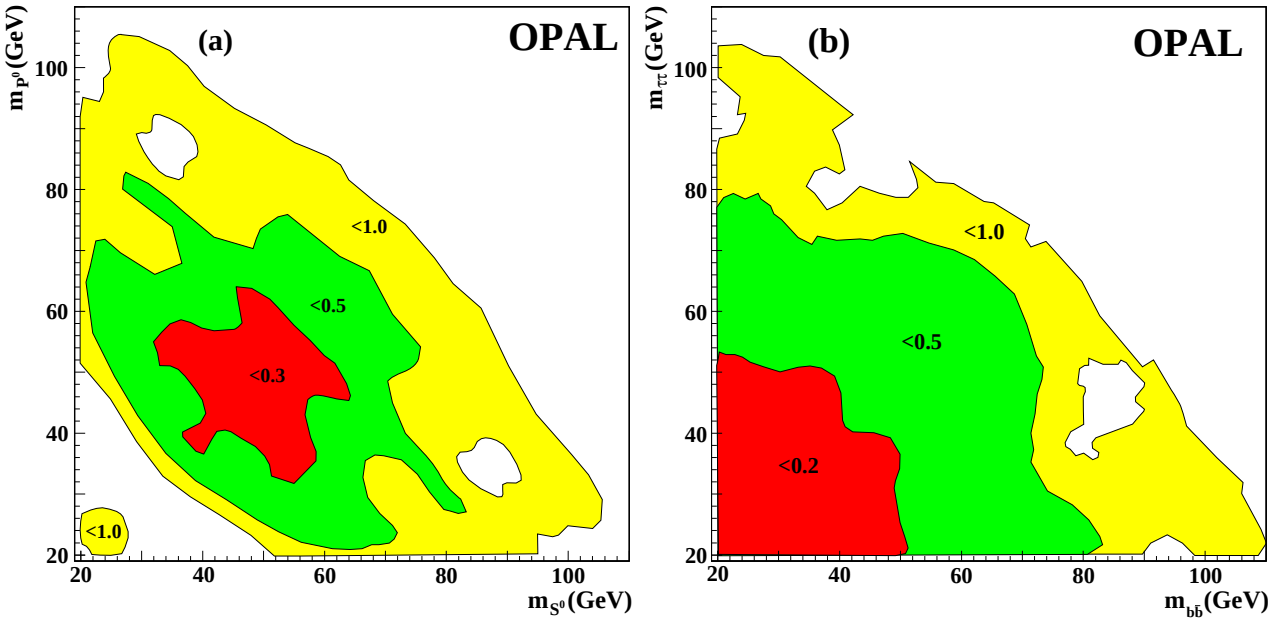

Figure 17: *Upper limits at 95% CL on c^2 (see Eq. (5)) for: (a) the $S^0P^0 \to b\bar{b}b\bar{b}$ search channel assuming the $b\bar{b}$ branching ratio for both S^0 and P^0 to be 100%, and (b) the $S^0P^0 \to b\bar{b}\tau^+\tau^-$ search channel assuming a 100% branching ratio for this final state. The invariant masses of the tau lepton pair and hadron jet pair are denoted $m_{\tau\tau}$ and $m_{b\bar{b}}$, respectively.*

channels and assumes SM Higgs branching ratios for the S^0. The dashed line (from a previous OPAL search [8] is computed assuming 100% hadronic branching ratio for the S^0 and uses only search channels that do not employ b-tagging (see [8] for a list of the search channels) and is therefore more general. At low masses, the searches lose sensitivity rapidly, and the limit for s^2 is determined from the decay width of the Z^0 boson only, as described in [8].

Figure 17 shows contours of 95% CL upper limits for c^2 in the S^0 and P^0 mass plane, for the processes $e^+e^- \to S^0P^0 \to b\bar{b}b\bar{b}$ and $b\bar{b}\tau^+\tau^-$, respectively. In both cases a 100% branching ratio into the specified final state is assumed. The contours are obtained from:

$$c^2 = \frac{N_{95}^{\mathrm{SP}}}{\sum\ (\epsilon\ \mathcal{L}\ \bar{\lambda}\ \sigma_{\nu\bar{\nu}}^{\mathrm{SM}})},$$

with N_{95}^{SP} being the 95% CL upper limit for the number of signal events in the data. The results obtained for $b\bar{b}b\bar{b}$ (Figure 17(a)) are symmetric with respect to interchanging S^0 and P^0. In Figure 17(b), the results for the $\tau^+\tau^-b\bar{b}$ final state are shown with the mass of the particle decaying into $\tau^+\tau^-$ along the abscissa and that of the particle decaying into $b\bar{b}$ along the ordinate. The irregularities of the contours are due to the presence of candidate events that affect N_{95}^{SP}.

In the 2HDM the bosons S^0 and P^0 are identified with h^0 and A^0, and the couplings s^2 and c^2 are identified with $\sin^2(\beta-\alpha)$ and $\cos^2(\beta-\alpha)$, respectively. The assignment of the possible excess width in Γ_Z to the process $Z^0 \to h^0Z^*$ yields an upper bound for s^2 which depends only on the mass of h^0 whereas the assignment to $Z^0 \to h^0A^0$ yields an upper bound for c^2 which depends on the masses of both h^0 and A^0. Combining these limits, the black region shown in Figure 18 is excluded at 95% CL regardless of the h^0 and A^0 decay modes. In the 2HDM, the most important final states of the decays of the h^0 and A^0 bosons are $b\bar{b}$, $c\bar{c}$ and $\tau^+\tau^-$ but

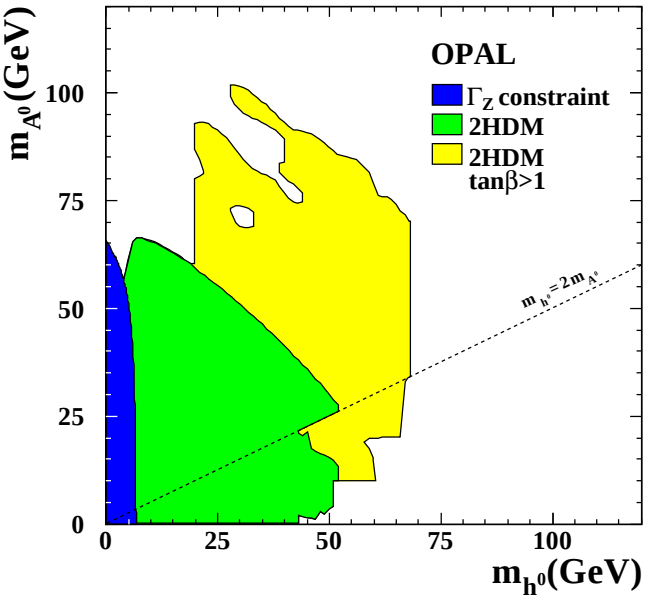

Figure 18: *Regions excluded at 95% CL in the Type II 2HDM. The black region is excluded using constraints from* Γ_Z *only. The dark grey region uses the direct searches for the SM Higgs in addition, but discarding the search channels that use b-tagging, assuming a hadronic branching ratio of the* h^0 *of 92%. The light grey region is excluded for* $\tan\beta > 1$ *in the 2HDM, assuming SM Higgs branching ratios for* h^0 *and* A^0*.*

$h^0 \to A^0A^0$ is also possible. The branching ratios depend on $\tan\beta$, but the hadronic branching fraction always exceeds 92% [44]. For $\tan\beta \geq 1$ the $b\bar{b}$ channel dominates while for $\tan\beta < 1$ the $c\bar{c}$ contribution may become the largest.

In Figure 18 the excluded area in the (m_{h^0}, m_{A^0}) plane is shown when the limits on c^2 and s^2 are combined. Below the dotted line, where the $h^0 \to A^0A^0$ decay is kinematically allowed and competes with the $h^0 \to f\bar{f}$ decay, the smaller of the detection efficiencies is used. The excluded area is therefore valid regardless of the $h^0 \to A^0A^0$ branching ratio. The dark grey area is excluded at 95% CL when $BR(h^0 \to q\bar{q}) \geq 92\%$ and is most generally valid in the 2HDM. This 95% CL limit is obtained using only search channels that do not employ b-tagging. The limit in the 2HDM for equal h^0 and A^0 masses is at $m_{h^0} = m_{A^0} = 41.0$ GeV. The light grey area is excluded when either SM Higgs branching ratios or $BR(h^0 \to A^0A^0) = 100\%$ is assumed for h^0 (whatever yields a more conservative result) and SM Higgs branching ratios are assumed for A^0. This assumption provides conservative results in the 2HDM for $\tan\beta > 1$. In that case, the 95% CL limit for equal h^0 and A^0 masses is at $m_{h^0} = m_{A^0} = 68.0$ GeV. The hole in the exclusion of the light grey area is caused by a candidate event in the $h^0A^0 \to b\bar{b}b\bar{b}$ search.

7.3 Interpretation of the Search Results within the MSSM

We consider a constrained MSSM with the following free parameters in addition to those of the SM. The model assumes unification of the scalar-fermion masses, m_0, at the grand unification (GUT) scale, and unification of the gaugino masses (parametrised using M_2, the SU(2) gaugino mass term at the electroweak scale) and unification of the scalar-fermion tri-linear couplings, A,

at the electroweak scale. The remaining parameters are chosen to be the supersymmetric Higgs mass parameter μ, the ratio of the vacuum expectation values of the two Higgs field doublets, $\tan\beta = v_2/v_1$, and the mass of the CP–odd Higgs boson, m_{A^0}. The above simplifications have practically no impact on the MSSM Higgs phenomenology; in particular, common scalar-fermion mass and tri-linear couplings are justified since only the scalar top ($\tilde{\mathrm{t}}$) sector gives important contributions to Higgs boson masses and couplings.

Those six parameters were scanned within ranges motivated by theory. The details of the MSSM parameter scans are described in [8]. Since the precise value of the top quark mass, m_{t}, has a strong impact through loop corrections (on m_{h^0} in particular), it was considered in the more general scans as a supplementary parameter, with values $m_{\mathrm{t}} = 165$, 175, and 185 GeV.

In this paper we consider the same three MSSM parameter scans (A, B and C) already used in [8].

Scan (A), proposed in [45], is the least general since, of the seven parameters (including m_{t}), only m_{A^0} and $\tan\beta$ are varied while m_0 and M_2 are fixed at 1 TeV and μ is chosen to be -100 GeV. The top quark mass is fixed at 175 GeV. Two sub-cases are considered, with the tri-linear coupling fixed at $A = 0$ TeV or $\sqrt{6}$ TeV, corresponding to *no mixing* or *maximal mixing* in the scalar-top sector. In *Scan (B)*, m_0, M_2, m_{A^0}, $\tan\beta$, and m_{t} are varied independently while μ and A are linked by relations which, in each case, correspond to either *minimal* or *maximal mixing* in the scalar-top sector. In *Scan (C)*, the most general, all seven parameters were varied independently. In each of these scans, the parameter sets were used as input to the HZHA program [22] which calculates the Higgs masses, cross–sections [46, 47] and branching ratios [44]. SUSYGEN [48] was used to calculate scalar fermion masses at the electroweak scale.

Parameter sets giving rise to chargino or neutralino masses [49], or stop masses [50], excluded by OPAL searches, or to $\mathrm{Z}^0 \to \mathrm{h}^0\mathrm{Z}^*, \mathrm{h}^0\mathrm{A}^0$ cross-sections incompatible with the Z^0 decay width (see [8]), have been discarded. In the case of scan (C), they were also tested against criteria [51, 52, 53] that exclude parameter sets leading to charge- or colour-breaking (CCB) minima of the MSSM Lagrangian.

The searches presented in this publication are combined with previous OPAL Higgs searches [7, 8, 42, 43] at $\sqrt{s}$ between m_{Z^0} and 172 GeV.

The results are presented, separately for each scan, in four sub-figures: (a) in the (m_{h^0}, m_{A^0}) plane for $\tan\beta > 1$, (b) in the same plane for $\tan\beta > 0.7$, (c) in the (m_{h^0}, $\tan\beta$) plane, and (d) in the (m_{A^0}, $\tan\beta$) plane. For scans (A) and (B) the experimental lower limits for the minimal and maximal mixing cases differ only marginally; therefore only the weaker of the two exclusion limits is given. The theoretically accessible area corresponds to the larger one, for maximal scalar top mixing. The theoretically inaccessible areas are shown in the figures in grey.

The results for scan (A) are shown in Figure 19. For $\tan\beta \geq 1$, the 95% CL lower limits obtained are $m_{\mathrm{h}^0} > 70.5$ GeV and $m_{\mathrm{A}^0} > 72.0$ GeV (Figure 19(a)). When the $\tan\beta$ range is enlarged to $\tan\beta > 0.7$ (Figure 19(b)), the lower limits on m_{h^0} and m_{A^0} are not affected, except for a small unexcluded region at $m_{\mathrm{A}^0} < 10$ GeV and 65 GeV $< m_{\mathrm{h}^0} <$ 72 GeV. In this region the searches for $\mathrm{h}^0 \to \mathrm{A}^0\mathrm{A}^0$ are not sensitive. For a detailed discussion of the region $m_{\mathrm{A}^0} < 5$ GeV see [8]. Figure 19(c) shows the projection onto the (m_{h^0}, $\tan\beta$) plane. For the specific parameter choices of scan (A), a region $0.8 < \tan\beta < 1.9$ can be excluded at 95% CL

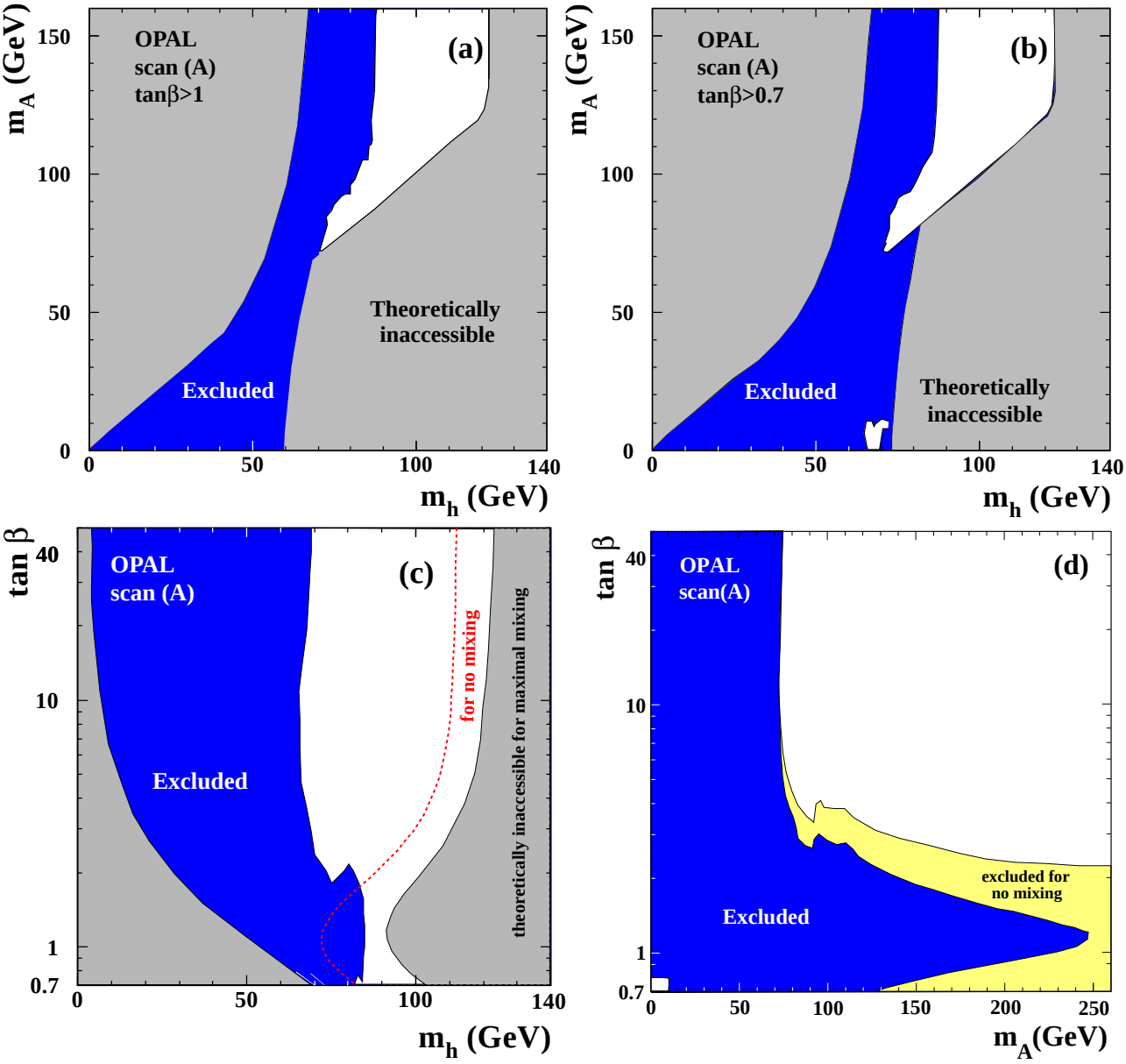

Figure 19: *The MSSM exclusion for scan (A) described in the text of Section 7.3. Excluded regions are shown for (a) the* (m_{h^0}, m_{A^0}) *plane for* $\tan\beta > 1$, *(b) the* (m_{h^0}, m_{A^0}) *plane for* $\tan\beta > 0.7$, *(c) the* (m_{h^0}, $\tan\beta$) *plane, and (d) the* (m_{A^0}, $\tan\beta$) *plane. The black area is excluded at 95% CL. The grey areas in (a), (b) and (c) are theoretically inaccessible. The light grey area in (d) is excluded only for no scalar-top mixing.*

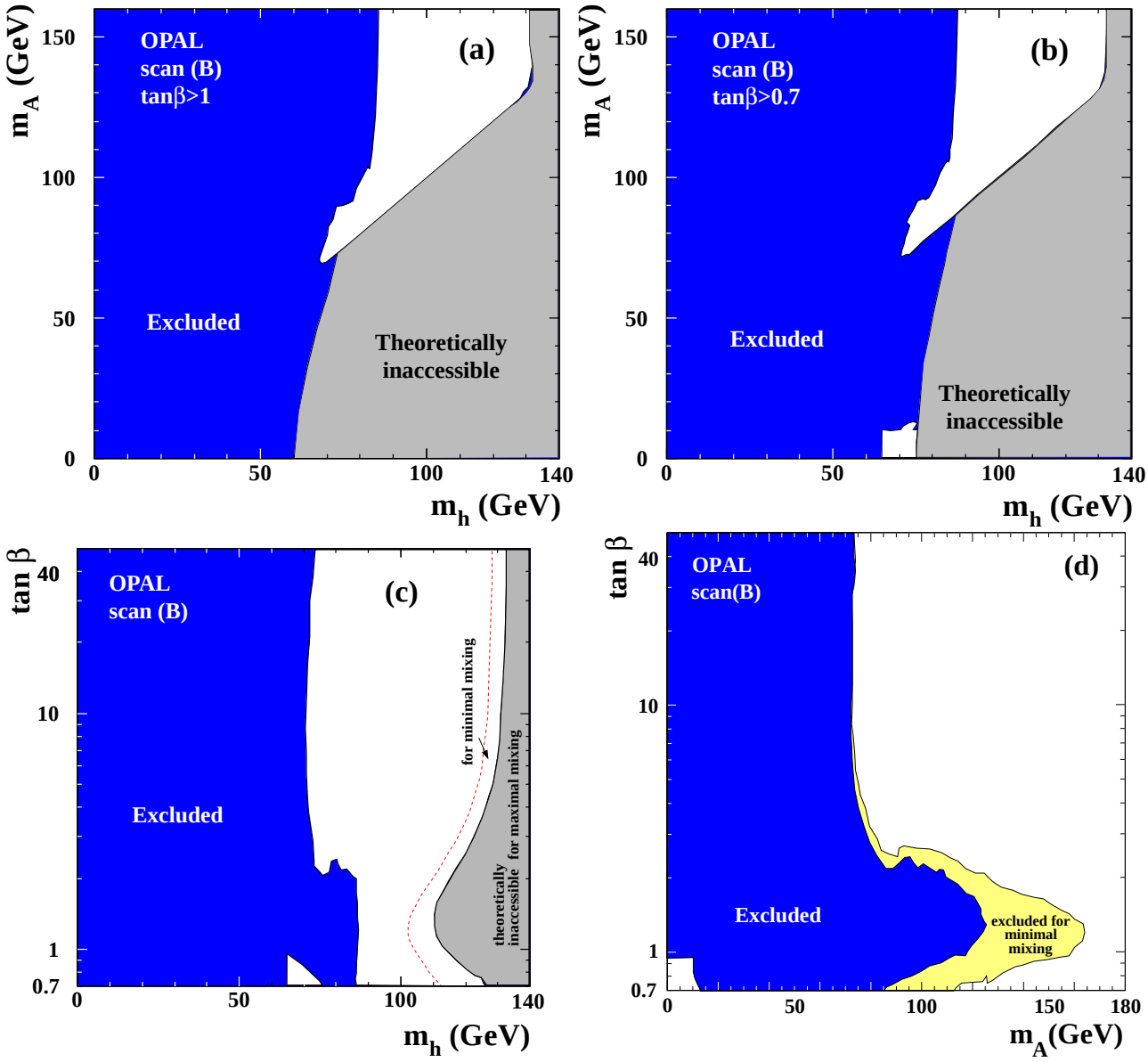

Figure 20: *The MSSM exclusion for the scan (B) described in the text of Section 7.3. Excluded regions are shown for (a) the (m_{h^0}, m_{A^0}) plane for* $\tan\beta > 1$, *(b) the (m_{h^0}, m_{A^0}) plane for* $\tan\beta > 0.7$, *(c) the (m_{h^0}, $\tan\beta$) plane, and (d) the (m_{A^0}, $\tan\beta$) plane. The black area is excluded at 95% CL. The grey areas in (a), (b) and (c) are theoretically inaccessible. The light grey area in (d) is excluded only for minimal scalar-top mixing.*

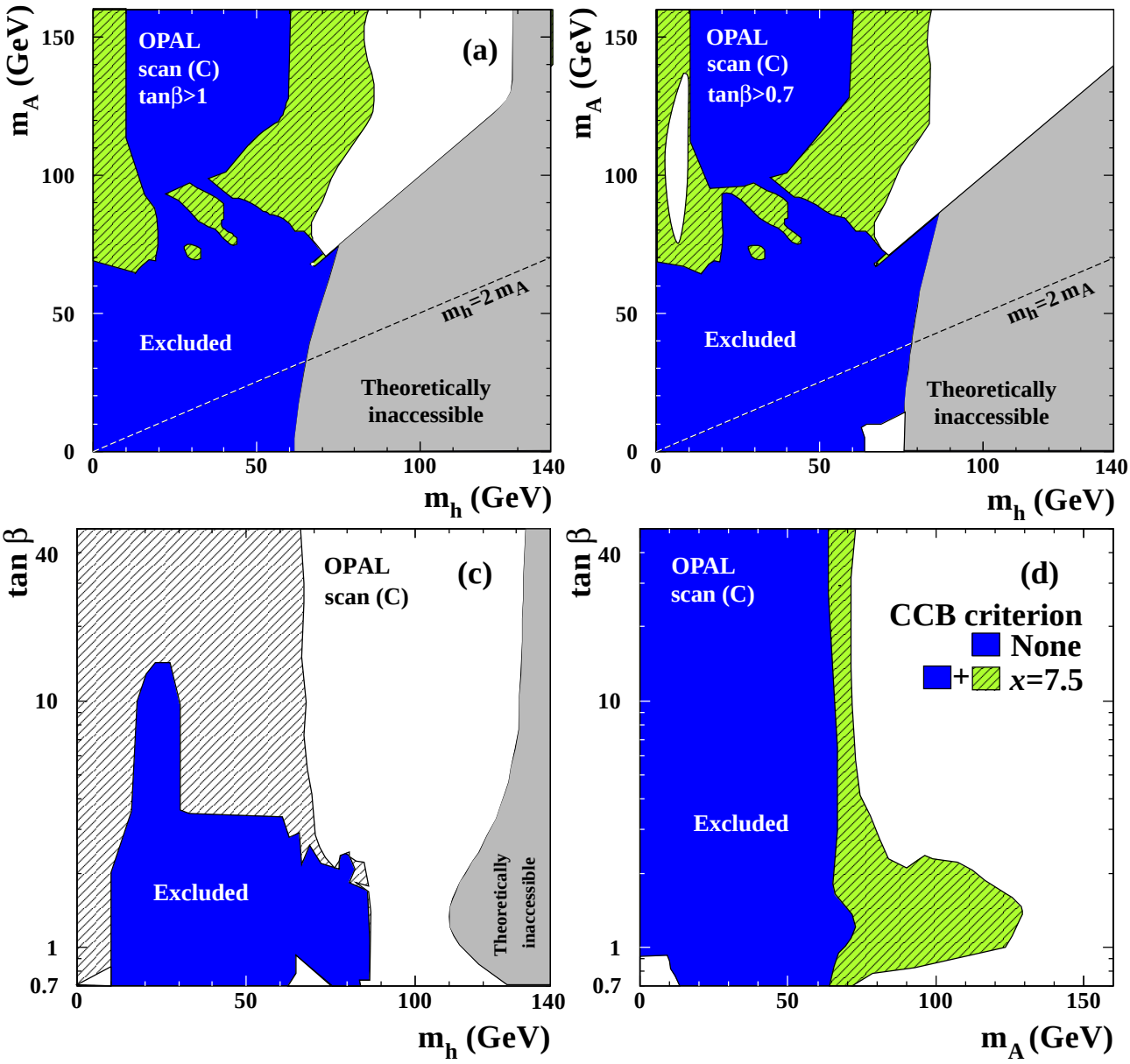

Figure 21: *The MSSM exclusion for scan (C) described in the text of Section 7.3. Excluded regions are shown for (a) the (m_{h^0}, m_{A^0}) plane for* $\tan\beta > 1$, *(b) the (m_{h^0}, m_{A^0}) plane for* $\tan\beta > 0.7$, *(c) the (m_{h^0}, $\tan\beta$) plane, and (d) the (m_{A^0}, $\tan\beta$) plane. All exclusion limits are at 95% CL. The black areas are excluded without applying any CCB criterion. When the CCB criterion is applied with* $x = 7.5$ *the grey hatched areas are excluded in addition. The grey areas in (a), (b) and (c) are theoretically inaccessible.*

for the case of no scalar-top mixing. Note, however, that this applies only for $m_{\rm top} \leq 175$ GeV. Since for larger top quark masses the theoretically allowed area widens significantly, no exclusion can be made in $\tan\beta$ e.g. for $m_{\rm t} = 185$ GeV. In Figure 19(d) the ($m_{\rm A^0}$, $\tan\beta$) projection is shown.

Figure 20 shows the results for scan (B). Differences with respect to scan (A) are due to the possibility of having lower $m_{\tilde{\rm t}}$ values. This leads in general to modified couplings and in particular, for some parameter sets, to a strongly enhanced branching ratio for $\rm h^0 \rightarrow gg$. The wider range of $m_{\tilde{\rm t}}$ in conjunction with $m_{\rm t} = 185$ GeV leads to larger theoretically accessible regions. Despite these modifications, many essential features such as the limit on $m_{\rm h^0}$ and $m_{\rm A^0}$ for $\tan\beta > 1$ (Figure 20(a)) remain unchanged. For $\tan\beta > 0.7$ (Figure 20(b)) the unexcluded region at low $m_{\rm A^0}$ becomes slightly larger, extending up to $m_{\rm A^0} \approx 13$ GeV. From Figures 20(c) and (d) it can be seen that an exclusion in $\tan\beta$ is no longer possible because of the larger theoretically allowed area.

The results for scan (C) are shown in Figure 21. The dark area is excluded at 95% CL. The grey hatched area is excluded if, in addition, a soft CCB criterion with $x = 7.5$ is applied as discussed in [8]. Lower values for x do not extend the exclusion. The exclusion in the low $\tan\beta$ region, $\tan\beta < 3$, is obtained by applying the SM search analysis also to $\rm Z^0H^0$ production, where $\rm H^0$ is the heavy CP-even Higgs boson. For $\tan\beta < 3$, the combination of $m_{\rm h^0} < 60$ GeV, $m_{\rm A^0} > 80$ GeV and very small $\sin^2(\beta - \alpha)$ typically leads to a heavy CP-even Higgs boson mass $m_{\rm H^0} < 90$ GeV, while $\rm Z^0H^0$ production is enhanced by the large $\cos^2(\beta - \alpha)$ value. As a consequence, the area of low $\tan\beta < 3$ and $10 < m_{\rm h^0} < 60$ GeV is excluded. However, as a side effect, an unexcluded region at $m_{\rm A^0} \approx m_{\rm h^0} \approx 67.5$ GeV and $m_{\rm H^0}$ close to 90 GeV appears for large $\tan\beta$ due to the presence of candidates. The unexcluded region at $m_{\rm h^0} < 10$ GeV and 75 GeV$< m_{\rm A^0} <$ 140 GeV for low $\tan\beta$ is a result of the limited sensitivity for $\rm Z^0h^0$ production for these $\rm h^0$ masses (see Figure 16).

For $\tan\beta > 1$ an absolute lower limit of $m_{\rm A^0} > 64.5$ GeV can be derived in the general scan at 95% CL. For $\tan\beta > 0.7$, the region 13 GeV $< m_{\rm A^0} < 64.5$ GeV is excluded at 95% CL, with no CCB criterion applied. When a soft CCB criterion is applied ($x = 7.5$) the mass limits at 95% CL are $m_{\rm A^0} > 67.5$ GeV and $m_{\rm h^0} > 67.5$ GeV, while for the latter also a region $m_{\rm h^0} < 10$ GeV is allowed if $\tan\beta < 0.85$.

7.4 Results of the Searches for Charged Higgs Bosons

Upper limits for the production cross-section times branching fraction of the decay into a given final state are presented in Figure 22(a). The results from various centre-of-mass energies are scaled to $\sqrt{s} = 183$ GeV, assuming the predicted s-dependence of the charged Higgs boson production cross-section.

Lower bounds on the mass of the charged Higgs boson are presented in Figure 22(b) as a function of the $\rm H^+ \rightarrow \tau^+\nu_\tau$ branching ratio. The expected mass limit from simulated background experiments (assuming no signals) is also shown. Charged Higgs bosons are excluded up to a mass of 59.5 GeV at 95% CL, independently of the $\rm H^+ \rightarrow \tau^+\nu_\tau$ branching ratio. For $BR(\rm H^+ \rightarrow \tau^+\nu_\tau) > 0.15$, a limit of 63.6 GeV can be set at 95% CL. Some regions are excluded by the searches in individual channels but not in their combination. This is mainly due to three

candidate events observed in the semileptonic channel around 66-68 GeV. All three events are consistent with W^+W^- production.

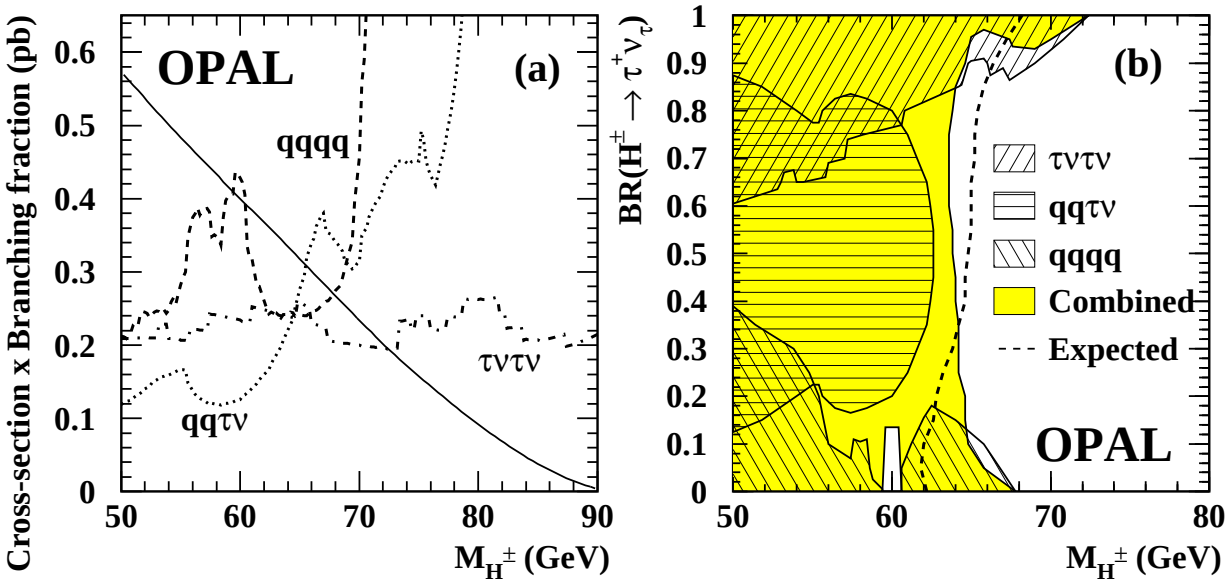

Figure 22: *(a) Upper limits at 95% CL, scaled to $\sqrt{s} = 183$ GeV, on the production cross-section times branching fraction of the decay for the process $e^+e^- \to H^+H^-$ for the three final states considered. Different centre-of-mass energies are combined, using the predicted s-dependence of the charged Higgs boson production cross-section. The charged Higgs boson production cross-section at $\sqrt{s} = 183$ GeV is shown as a solid line. Note that the maximum branching fraction for the $\tau^+\nu_\tau q\overline{q}'$ final state is 0.5. (b) Excluded areas at 95% CL in the $[M_{H^\pm}, BR(H^+ \to \tau^+\nu_\tau)]$ plane. The results from each of the channels separately are indicated by different hatch styles, and the combined exclusion by the shaded area. The dashed line shows the expected 95% CL limit from simulated background experiments.*

8 Summary

The searches for Higgs bosons presented here and based on data collected by OPAL at $\sqrt{s}$= 183 GeV, have not revealed any significant excess over the expected backgrounds. In combination with previous search results, new limits on the masses of neutral and charged Higgs bosons have been set at 95% CL. In particular, the Standard Model Higgs boson is excluded for masses below 88.3 GeV. In the MSSM, for parameter sets corresponding to minimal and maximal scalar top mixing, masses of m_{A^0} (m_{h^0}) below 72.0 GeV (70.5 GeV) are excluded for $\tan\beta > 1$. For minimal scalar top mixing, soft SUSY breaking masses of 1 TeV, and $m_{\rm top} \leq 175$ GeV, the range $0.8 < \tan\beta < 1.9$ is excluded. If the MSSM parameters are varied in a general scan, masses of A^0 and h^0 below 67.5 GeV are excluded for $\tan\beta > 1$. Charged Higgs bosons are excluded below 59.5 GeV.

Acknowledgements

We particularly wish to thank the SL Division for the efficient operation of the LEP accelerator at all energies and for their continuing close cooperation with our experimental group. We thank our colleagues from CEA, DAPNIA/SPP, CE-Saclay for their efforts over the years on the time-of-flight and trigger systems which we continue to use. In addition to the support staff at our own institutions we are pleased to acknowledge the
Department of Energy, USA,
National Science Foundation, USA,
Particle Physics and Astronomy Research Council, UK,
Natural Sciences and Engineering Research Council, Canada,
Israel Science Foundation, administered by the Israel Academy of Science and Humanities,
Minerva Gesellschaft,
Benoziyo Center for High Energy Physics,
Japanese Ministry of Education, Science and Culture (the Monbusho) and a grant under the Monbusho International Science Research Program,
Japanese Society for the Promotion of Science (JSPS),
German Israeli Bi-national Science Foundation (GIF),
Bundesministerium für Bildung, Wissenschaft, Forschung und Technologie, Germany,
National Research Council of Canada,
Research Corporation, USA,
Hungarian Foundation for Scientific Research, OTKA T-016660, T023793 and OTKA F-023259.

Appendix: Lifetime Tag

The five quantities which are input to an artificial neural network (ANN) to form the lifetime tag for b-flavour, β_τ, are described here.

The first three of these quantities rely on the reconstruction of secondary vertices. Within a jet, sub-jets are formed using a cone algorithm [54] with a cone half angle of 0.5 radians and a minimum sub-jet energy of 7 GeV. In each of these sub-jets, a secondary vertex is reconstructed using the method described in [55]. In order to compensate for the loss in b-tagging efficiency due to the requirement of secondary vertex reconstruction, the last two of the inputs to the ANN are based on track impact parameters only.

The quantities are the following:

(1) Secondary vertex likelihood, $\mathcal{L}_S$: a vertex-multiplicity-dependent likelihood $\mathcal{L}_S$ is formed using the decay length significance, S (the decay length divided by its error). $\mathcal{L}_S$ is calculated from the probability density function (p.d.f.) of S for b, c and uds flavours, $f_{\rm b}$, $f_{\rm c}$, $f_{\rm uds}$. If more than one sub-jet is formed, the secondary vertex with the largest $\mathcal{L}_S$ in a given jet is selected for this and the following two quantities.

(2) Reduced secondary vertex likelihood, $\mathcal{L}_R$: the reduced decay length is obtained from a

vertex fit using all tracks in the secondary vertex, except the one with the largest impact parameter significance, i.e., the impact parameter with respect to the primary vertex divided by its error. While for b-flavoured hadron decays, the reduced decay length often coincides with the decay length, randomly formed vertices are less robust against removing the most significant track. The reduced decay length significance R is given by the reduced decay length divided by its error. From R a multiplicity-dependent likelihood $\mathcal{L}_R$ is calculated. If a secondary vertex consists of only two tracks, R is not defined. In that case, $\mathcal{L}_R$ is set to the value corresponding to the likelihood for b-flavour to form a reconstructed two track vertex relative to all flavours.

(3) Critical track discriminator, $T_{\rm crit}$: An auxiliary ANN is trained to discriminate between tracks originating from the b-flavoured hadron decay and from tracks due to fragmentation or decays of light-flavoured hadrons. The inputs to this ANN are the impact parameter of the track with respect to the primary vertex, the impact parameter with respect to the secondary vertex, the momentum of the track, and its transverse momentum with respect to the corresponding sub-jet axis. The tracks belonging to the sub-jet are then sorted according to the output of the auxiliary ANN in a descending order. Tracks are added one by one to a 'cluster' of tracks whose invariant mass is calculated, assuming that all tracks have the pion mass. $T_{\rm crit}$ is the auxiliary ANN output of that track which causes the cluster invariant mass to exceed 1.9 GeV. This algorithm exploits the higher mass of b-flavoured hadrons compared to charmed and lighter hadrons. The algorithm is described in detail in [34].

(4) Two-dimensional impact parameter joint probability, ($P_{\rm join}$): The impact parameter distribution for tracks with negative impact parameter significance[6] is assumed to represent the class of tracks from the primary vertex and thus provides an estimate of the detector resolution function. This resolution function is then used to "weight" the tracks, and the joint probability for the tracks in a jet to come from the primary vertex is given by

$$P_{\rm join} = y \sum_{m=0}^{N-1} \frac{(-\ln y)^m}{m!},$$

where y is the product of the probabilities of all N tracks with positive impact parameters in the jet [56]. Only tracks that pass stringent track quality criteria are used in the calculation of $P_{\rm join}$.

(5) Impact parameter mass tag ($P_{\rm mass}$): Tracks in each sub-jet are sorted in descending order of the impact parameter significance and iteratively clustered. $P_{\rm mass}$ is defined as the impact parameter significance of that track which causes the invariant mass of the cluster to exceed 1.2 GeV. When more than one sub-jet is reconstructed in a given jet, the highest $P_{\rm mass}$ value is used. Only tracks that pass stringent track quality criteria are used in the calculation of $P_{\rm mass}$.

The five variables $\mathcal{L}_S$, $\mathcal{L}_R$, $T_{\rm crit}$, $P_{\rm join}$ and $P_{\rm mass}$ are then input to an ANN. Monte Carlo samples at $\sqrt{s} = m_{Z^0}$ are used to train the ANN. The program JETNET 3.4 [57] is used with

[6]The impact parameter is taken to be positive if, in the two-dimensional projection, the track path, starting from the point of closest approach to the primary vertex, crosses the jet axis in the flight direction; otherwise it is negative.

five input nodes, one hidden layer with 10 nodes and one output node, the lifetime-tag β_τ. Since the vertex tagging performance depends on the jet polar angle, three separate ANN's are trained for jets with $|\cos\theta_{\rm jet}| \leq 0.75$, $0.75 < |\cos\theta_{\rm jet}| \leq 0.9$, and $|\cos\theta_{\rm jet}| > 0.9$.

References

[1] S.L. Glashow, J. Iliopoulos, and L. Maiani, Phys. Rev. **D2** (1970) 1285;
S. Weinberg, Phys. Rev. Lett. **19** (1967) 1264;
A. Salam, *Elementary Particle Theory*, ed. N. Svartholm (Almquist and Wiksells, Stockholm, 1968), 367.

[2] J.F. Gunion, H.E. Haber, G.L. Kane, and S. Dawson, *The Higgs Hunter's Guide*, Addison-Wesley Publishing Company, Reading, MA, 1990.

[3] H.P. Nilles, Phys. Rep. **110** (1984) 1;
H.E. Haber and G.L. Kane, Phys. Rep. **117** (1985) 75;
R. Barbieri *et al.*, *Z Physics at LEP1*, CERN 89-08 (1989) Vol. 2, 121;
J.M. Frère and G.L. Kane, Nucl. Phys. **B223** (1983) 331;
J. Ellis *et al.*, Phys. Lett. **B123** (1983) 436;
J. Ellis *et al.*, Phys. Lett. **B127** (1983) 233.

[4] P.W. Higgs, Phys. Lett. **12** (1964) 132;
F. Englert and R. Brout, Phys. Rev. Lett. **13** (1964) 321;
G.S. Guralnik, C.R. Hagen, and T.W.B. Kibble, Phys. Rev. Lett. **13** (1964) 585.

[5] M. Carena, J.R. Espinosa, M. Quirós, and C.E.M. Wagner, Phys. Lett. **355B** (1995) 209.

[6] A. Akeroyd *et al.*, Nucl. Phys. **B529** (1998) 3.

[7] OPAL Collaboration, K. Ackerstaff *et al.*, Eur. Phys. J. **C1** (1998) 425.

[8] OPAL Collaboration, K. Ackerstaff *et al.*, Eur. Phys. J. **C5** (1998) 19.

[9] OPAL Collaboration, K. Ackerstaff *et al.*, Phys. Lett. **B426** (1998) 180.

[10] ALEPH Collaboration, R. Barate *et al.*, Phys. Lett. **B412** (1997) 155;
ALEPH Collaboration, R. Barate *et al.*, Phys. Lett. **B412** (1997) 173;
DELPHI Collaboration, P. Abreu *et al.*, Eur. Phys. J.**C2** (1998) 1;
L3 Collaboration, M. Acciarri *et al.*, Phys. Lett. **B431** (1998) 437;
L3 Collaboration, M. Acciarri *et al.*, *Search for Neutral Higgs Bosons of the Minimal Supersymmetric Standard Model in e+ e- Interactions at s**(1/2) = 130 GeV - 183 GeV*, CERN-EP-98-072, submitted to Phys. Lett. B.

[11] Aleph Collaboration, R. Barate *et al.*, Phys. Lett. **B418** (1998) 419;
DELPHI Collaboration, P. Abreu *et al.*, Phys. Lett. **B420** (1998) 140;
L3 Collaboration, M. Acciarri *et al.*, *Search for Charged Higgs Bosons in e+e- Collisions at Centre-of-Mass Energies between 130 and 183 GeV*, CERN-EP/98-149, submitted to Phys. Lett. B.

[12] CLEO Collaboration, M.S. Alam *et al.*, Phys. Rev. Lett. **74** (1995) 2885.

[13] CDF Collaboration, F. Abe *et al.*, Phys. Rev. Lett. **79** (1997) 357.

[14] ALEPH, DELPHI, L3, and OPAL collaborations, and the LEP Working Group for Higgs Boson Searches, *Bound for the Standard Model Higgs Boson Mass from Combining the Results of the four LEP Experiments*, CERN-EP/98-046.

[15] OPAL Collaboration, K. Ahmet *et al.*, Nucl. Inst. and Meth. **A305** (1991) 275.

[16] S. Anderson *et al.*, Nucl. Inst. and Meth. **A403** (1998) 326.

[17] OPAL Collaboration, K. Ackerstaff *et al.*, *Search for Acoplanar Lepton Pair Events in* e^+e^- *Annihilation at* $\sqrt{s}$ *= 161, 172 and 183 GeV*, CERN-EP/98-122, submitted to Eur. Phys. J. **C**.

[18] B.E. Anderson *et al.*, IEEE Transactions on Nuclear Science **41** (1994) 845.

[19] OPAL Collaboration, K. Ackerstaff *et al.*, Phys. Lett. **B391** (1997) 221.

[20] OPAL Collaboration, R. Akers *et al.*, Phys. Lett. **B327** (1994) 397.

[21] OPAL Collaboration, K. Ackerstaff *et al.*, Eur. Phys. J. **C2** (1998) 213.

[22] HZHA generator: P. Janot, *Physics at LEP2*, CERN 96-01 (1996), Vol.2, 309.

[23] PYTHIA 5.721 and JETSET 7.408 generators: T. Sjöstrand, Comp. Phys. Comm. **82** (1994) 74; T. Sjöstrand, LU TP 95-20.

[24] EXCALIBUR generator: F.A. Berends, R. Pittau, and R. Kleiss, Comp. Phys. Comm. **85** (1995) 437.

[25] The grc4f 1.1 generator: J. Fujimoto *et al.*, Comp. Phys. Comm. **100** (1997) 128.
J. Fujimoto *et al.*, *Physics at LEP2*, CERN 96-01 (1996), Vol.2, 30.

[26] BHWIDE generator: S. Jadach, W. Płaczek, and B.F.L. Ward, *Physics at LEP2*, CERN 96-01 (1996), Vol.2, 286; UTHEP-95-1001.

[27] KORALZ 4.0 generator: S. Jadach, B.F.L. Ward, and Z. Wąs, Comp. Phys. Comm. **79** (1994) 503.

[28] PHOJET 1.05 generator: E. Budinov *et al.*, *Physics at LEP2*, CERN 96-01 (1996), Vol.2, 216;
R. Engel and J. Ranft, Phys. Rev. **D54** (1996) 4244.

[29] G. Marchesini *et al.*, Comp. Phys. Comm. **67** (1992) 465.

[30] J.A.M. Vermaseren, Nucl. Phys. **B229** (1983) 347.

[31] OPAL Collaboration, G. Alexander *et al.*, Z. Phys **C69** (1996) 543.

[32] J. Allison *et al.*, Nucl. Inst. and Meth. **A317** (1992) 47.

[33] OPAL Collaboration, G. Alexander *et al.*, Z. Phys. **C70** (1996) 357.

[34] OPAL Collaboration, K. Ackerstaff *et al.*, *A Measurement of R_b using a Double Tagging Method* CERN-EP/98–137; submitted to Eur. Phys. J. **C**

[35] OPAL Collaboration, K. Ackerstaff *et al.*, Eur. Phys. J. **C2** (1998) 441.

[36] N. Brown and W.J. Stirling, Phys. Lett. **B252** (1990) 657;
S. Bethke, Z. Kunszt, D. Soper and W.J. Stirling, Nucl. Phys. **B370** (1992) 310;
S. Catani *et al.*, Phys. Lett. **B269** (1991) 432;
N. Brown and W.J. Stirling, Z. Phys. **C53** (1992) 629.

[37] G. Parisi, Phys. Lett. **B74** (1978) 65;
J.F. Donoghue, F.E. Low and S.Y. Pi, Phys. Rev. **D20** (1979) 2759.

[38] OPAL Collaboration, R. Akers *et al.*, Z. Phys. **C61** (1994) 209;
DELPHI Collaboration, P. Abreu *et al.*, Phys. Lett. **B347** (1995) 447.

[39] ALEPH Collaboration, D. Buskulic *et al.*, Phys. Lett. **B357** (1995) 699;
ALEPH Collaboration, D. Buskulic *et al.*, Z. Phys. **C62** (1994) 179;
DELPHI Collaboration, P. Abreu *et al.*, Z. Phys. **C66** (1995) 323;
OPAL Collaboration, R. Akers *et al.*, Z. Phys. **C60** (1993) 199;
OPAL Collaboration, G. Alexander *et al.*, Phys. Lett. **B364** (1995) 93.

[40] R.A. Davis, *Search for a Standard Model Higgs Boson in 161 GeV Electron Positron Collisions Using Neural Networks*, University of Alberta M.Sc. Thesis, Spring 1997 (unpublished).

[41] OPAL Collaboration, K. Ackerstaff *et al.*, Eur. Phys. J. **C1** (1998) 395;
OPAL Collaboration, K. Ackerstaff *et al.*, Phys. Lett. **B389** (1996) 416.

[42] OPAL Collaboration, G. Alexander *et al.*, Z. Phys. **C73** (1997) 189.

[43] OPAL Collaboration, R. Akers *et al.*, Z. Phys. **C64** (1994) 1.

[44] A. Djouadi, J. Kalinowski and M. Spira, Comp. Phys. Comm. **108** (1998) 56.

[45] E. Accomando *et al.*, in *Physics at LEP2*, CERN 96-01 (1996), Vol.1, 351.

[46] F.A. Berends and R. Kleiss, Nucl. Phys. **178** (1981) 141.

[47] E. Gross, B.A. Kniehl and G. Wolf, Z. Phys. **C63** (1994) 417;
erratum *ibid.* **C66** (1995) 32.

[48] E. Accomando *et al.*, in *Physics at LEP2*, CERN 96-01 (1996), Vol.2, 299.

[49] OPAL Collaboration, K. Ackerstaff *et al.*, *Search for Chargino and Neutralino Production at $\sqrt{s}$= 181-184 GeV at LEP*, CERN-EP/98-136, to be published in Eur. Phys. J. **C**.

[50] OPAL Collaboration, K. Ackerstaff *et al.*, Z. Phys. **C75** (1997) 409.

[51] J.M. Frère, D.R.T. Jones and S. Raby, Nucl. Phys. **B222** (1983) 11;
L. Alvarez-Gaumé, J. Polchinski and M. Wise, Nucl. Phys. **B221** (1983) 495;
J.P. Derendinger and C.A. Savoy, Nucl. Phys. **B237** (1984) 307;
C. Kounnas, A.B. Lahanas, D.V. Nanopoulos and M. Quirós, Nucl. Phys. **B236** (1986) 438.

[52] J.A. Casas, A. Lleyda and C. Muñoz, Nucl. Phys. **B471** (1996) 3. J.A. Casas and S. Dimopoulos, Phys. Lett. **B387** (1996) 107.

[53] A. Kusenko, P. Langacker and G. Segre, Phys. Rev. **D54** (1996) 5824.

[54] OPAL Collaboration, R. Akers *et al.*, Z. Phys **C63** (1994) 197.

[55] OPAL Collaboration, K. Ackerstaff *et al.*, Z. Phys. **C74** (1997) 1;
OPAL Collaboration, R. Akers *et al.*, Z. Phys. **C66** (1995) 19.

[56] ALEPH Collaboration, R. Barate *et al.*, Phys. Lett. **B 412** (1997) 173.

[57] JETNET 3.0 program: C. Peterson, T. Rögnvaldsson, and L. Lönnblad, Comp. Phys. Comm. **81** (1994) 185.